NGR-05-002-160

N73-33777

CASE FILE COPY

A SATELLITE MEASUREMENT OF COSMIC-RAY ABUNDANCES AND SPECTRA IN THE CHARGE RANGE $2 \leq Z \leq 10$

Thesis by

James William Brown

CALIFORNIA INSTITUTE OF TECHNOLOGY

A SATELLITE MEASUREMENT OF COSMIC-RAY ABUNDANCES AND SPECTRA IN THE CHARGE RANGE $2 \leq Z \leq 10$

Thesis by

James William Brown

SRL 73-2

June 1973

A SATELLITE MEASUREMENT OF COSMIC-RAY ABUNDANCES AND SPECTRA IN THE CHARGE RANGE $2 \leq Z \leq 10$

Thesis by

James William Brown

In Partial Fulfillment of the Requirements

for the Degree of

Doctor of Philosophy

California Institute of Technology

Pasadena, California

1974

(Submitted June 12, 1973)

ACKNOWLEDGMENTS

Many people have contributed a great deal toward the completion of the research described in this thesis. Foremost among these has been my faculty advisor, Professor Edward Stone, whose seemingly boundless energy and enthusiasm and considerable insight into physical and administrative processes have been invaluable assets. I have also profited from Professor Rochus Vogt's comments about physics and physicists.

The Caltech experiment on OGO-6 was designed and built through the efforts of the staffs of the Caltech Space Radiation Laboratory, Central Engineering Services, and the Analog Technology Corporation. Dr. Stephen Murray was responsible for the prelaunch testing and extensive calibration of the instrument, and the design of the early phases of the data manipulation process.

Mrs. Hannah Fox implemented the first versions of the data tape abstraction program. The tedious processes of tape abstraction, bookkeeping, reprocessing, and editing were ably performed by Mrs. Ellen Aguilar and Mrs. Florence Pickett, and especially by Mr. Gary Pope.

Dr. Margaret Shea of Air Force Cambridge Research Laboratories supplied us with the results of extensive calculations of geomagnetic cutoffs, without which the analysis described in this thesis would not have been possible. I am also indebted to Dr. Jean Audouze who gave us a copy of his program which calculates interstellar propagation effects, complete with his latest compilation of production cross sections. Dr. Catherine Cesarsky and Mr. Solomon Vidor contributed substantially to my understanding of the subtleties of the propagation calculation.

The program which calculates the effects of solar modulation was supplied, along with helpful comments, by Dr. Thomas Garrard, who was a valuable source of advice throughout the course of this research.

I wish to thank Mrs. Elinor Murphy and Mrs. Marty Neale for typing the first draft of parts of this thesis. I would also like to express special appreciation for the fine workmanship and courteous service of the staff of Graphic Arts, especially Miss Pat Lee and Mr. Burt Bailey.

During my graduate study I have received financial support from the National Science Foundation and the California Institute of Technology. The research described in this thesis was supported by the National Aeronautics and Space Administration under contract NAS5-9312 and grant NGR-05-002-160.

ABSTRACT

The composition of the nuclear component of the cosmic radiation has been under study for some time, because it can yield information concerning the source, propagation, and confinement of cosmic rays within the galaxy. We present here the first comprehensive satellite measurement of cosmic-ray composition and spectra in the charge range $2 \leq Z \leq 10$ using the geomagnetic field as a rigidity analyzer through the entire range of vertical cutoffs. The results indicate that the spectra of all the elements in the observed range are similar, and thus that various ratios of elemental abundances are nearly independent of rigidity over the range $2 \lesssim P \lesssim 15$ GV. Calculations of the propagation of cosmic rays through the interstellar and interplanetary media predict that there should be a variation with rigidity of ratios of various elements, because of the charge-dependent effects of ionization of the interstellar gas by the cosmic rays. The absence of this variation can be explained by assuming a rigidity-dependent confinement of the cosmic rays in the galaxy. From the ratios Be/O and B/O we obtain a leakage mean free path decreasing from $\sim$10 g/cm^2 at $\sim$2 GV to $\sim$6-7 g/cm^2 at 10-15 GV, assuming that the interstellar gas is composed of hydrogen and helium in a 10:1 ratio. Ratios of other cosmic-ray elements are consistent with such a decreasing path length. The confinement time of the cosmic rays in the galaxy can be estimated from the ratio Be/B, because of the radioactive decay of ^{10}Be to ^{10}B. The data indicate a confinement time of $10^{6.5\pm0.5}$ years, which may be rigidity-dependent.

to Macrine

for her patience, encouragement, and help

Table of Contents

I. Introduction 1

II. Experiment

A. Spacecraft 5

B. Čerenkov Telescope 5

C. Calibrations 12

III. Data

A. Event Selection Criteria 25

B. Charge, Velocity Assignment 40

C. Abundance Ratios 50

IV. Results and Interpretation

A. Integral Rigidity Spectra 55

B. Abundance Ratios and Interstellar Propagation 67

V. Summary and Conclusions 87

Appendix A. Data Processing and Assignment of Cutoff Rigidities 89

Appendix B. Identification of Geomagnetically Trapped Particles 92

References 107

I. Introduction

Ever since the discovery (*Freier et al.*, 1948) of nuclei heavier than protons in the cosmic radiation, considerable effort has been expended in making measurements of the elemental composition and the energy spectra of this component of the cosmic rays, and in developing models to account for the observations. The current picture of the production of the heavy nuclei can be outlined as follows. A source, or a number of sources, injects into the galactic medium a flux of high energy nuclei. The composition of this flux depends on the composition of the source region, but it is presumed to contain primarily protons, α-particles, and those nuclei (such as ^{12}C, ^{16}O, ^{20}Ne, ^{24}Mg, ^{28}Si, ^{56}Fe) which are expected to be produced abundantly in various thermonuclear processes which presumably have produced the source material. These high-energy particles propagate within the galaxy, guided by the interstellar magnetic field. Because of random irregularities in this field, the particles diffuse throughout the galaxy, and may escape when they reach the boundary. During their travel, they may interact with atoms of the interstellar gas, which is composed mainly of hydrogen. They may ionize the atoms of the gas, in which case they lose energy to the atomic electrons, and they may suffer nuclear interactions in which they are transmuted into lighter nuclei. By this latter process, nuclei are formed which may not have been present at the source. Thus, by measuring the composition near earth, we can deduce some of the characteristics of the propagation, and, given enough data and adequate models, we can also learn something about the sources. For instance, a knowledge of the confinement time and the energy density of the cosmic rays provides

information on the overall source strength.

Recently, the advent of many new technologies has brought this field to the point where detailed comparisons of theory and experiment are possible. Some of the recent developments which have been very useful are: solid-state detectors (silicon and large-area crystal and plastic scintillators), rugged, sensitive photomultiplier tubes, improved detectors for Čerenkov radiation, and superconducting magnets, as well as large, high-altitude balloons and, of course, artificial satellites. An excellent review of the recent status of the measurements and theoretical implications was published by Shapiro and Silberberg (1970).

Most of the measurements of composition and spectra have been made by experiments flown on high-altitude balloons (*e.g., Webber and Ormes,* 1967; *Corydon-Petersen et al.,* 1970; *Smith et al.,* 1973; and many others). Experiments of this type can be quite large and massive, providing the large collection factors needed to obtain good statistics from the rather low particle fluxes, and allowing determination of particle energies or rigidities up to quite high values (*e.g.,* rigidity $\gtrsim$ 100 GV). However, these experiments are shielded from direct exposure to the cosmic rays by several g/cm^2 of overlying atmosphere. Ionization and nuclear interactions in the air above the experiment produce distortions in the spectra and composition of the radiation, requiring corrections which may introduce a certain amount of uncertainty into the results.

This problem can be avoided by making the observations on satellites outside the atmosphere. The difficulties here are imposed by the necessarily small size of most satellite experiments. In order to obtain adequate counting statistics, data must be taken for periods on the order

of months or years, requiring considerable stability and reliability of the instrument. Also, it is difficult to make determinations of energy above $\sim$ 1 GeV/nucleon, due to the small size and mass available for experiments. As a result, most satellite measurements are restricted to energies below a few hundred MeV/nucleon (*e.g.*, *Balasubrahmanyan et al.*, 1966; *Comstock et al.*, 1966). This can be extended to $\sim$ 1 GeV/nucleon by using a Čerenkov detector in addition to the usual dE/dx and total- E detectors (*Lezniak and Webber*, 1969; *Teegarden et al.*, 1970; *Mason*, 1972).

It has been known for quite some time (*Orear et al.*, 1949; *Störmer*, 1955 and references therein) that the geomagnetic field prevents some particles from reaching the top of the atmosphere. The simplest model of the process, using a dipole field and ignoring the presence of the solid earth, predicts that particles having a magnetic rigidity (momentum/charge) below a certain cutoff value cannot be incident at the surface of the earth. For vertically incident particles, the cutoff is given simply by

$$P_c = P_0 \cos^4 \lambda \qquad \text{(I-1)}$$

where λ is the magnetic dipole latitude, and $P_0 \simeq 15$ GV (rigidity is commonly defined as pc/Ze and measured in volts; 1 GV = 10^9 volts). Thus the geomagnetic field can be used to determine threshold rigidities up to $\sim$ 15 GV, depending on latitude, enabling one to determine spectra up to that rigidity. The actual calculation of cutoff rigidities is considerably more complex, however, than is indicated by Equation I-1.

The method used is described in Appendix A.

We describe in this thesis the first satellite measurement of cosmic ray elemental composition using the geomagnetic field as a spectral analyzer, through the entire range of vertical cutoffs from zero to ∿15 GV. Techniques of data analysis are described which yield a charge resolution of ∿0.2 charge unit. Integral rigidity spectra are presented, as well as ratios of various elements. The results are discussed in relation to a steady-state model for propagation and confinement of cosmic rays within the galaxy.

II. Experiment

A. Spacecraft

The Caltech Solar and Galactic Cosmic Ray Experiment (*Althouse et al.*, 1967) was launched into a polar orbit aboard the OGO-6 spacecraft on June 5, 1969. The initial orbit parameters were: perigee 397 km, apogee 1098 km, inclination 82°, period 99.8 min (OGO Experiment Bulletin F-143). The data used in this thesis were taken during the period June 7, 1969 to August 28, 1970.

The low-altitude polar orbit of OGO-6 provided extensive sampling of the entire range of vertical geomagnetic cutoff rigidities up to $\sim$15 GV. In addition, the spacecraft was oriented so the Caltech experiment is always facing radially away from the earth.

B. Čerenkov Telescope

At moderately high energies, i.e., above a few hundred MeV/nucleon, a useful technique for charged-particle measurements is a simultaneous determination of ionization energy loss in a thin detector and of Čerenkov radiation in a material of suitable index of refraction, n. If the particle velocity β is greater than 1/n, then the number of Čerenkov photons emitted is proportional to $Z^2\,[1-(\beta n)^{-2}]$, where Z is the charge. The particle's energy loss in a thin detector is approximately proportional to Z^2/β^2. Thus a simultaneous measurement of these two quantities can be used to determine both the charge and velocity of the particle.

A cross section of the Čerenkov Telescope is shown in Figure II-1. D1' and D2' are totally depleted Au-Si surface barrier detectors, nominally 1 mm thick, with diameters of ∿2.34 cm. D3' is the 1 cm thick fused silica window of a 2-inch photomultiplier tube. D4' is a plastic scintillator anticoincidence shield. A D2'D3'$\overline{D4'}$ coincidence is required for event analysis. Particle energy loss (-dE/dx) is measured in D1' and D2', and pulse-height analyzed over a range from ∿100 keV to ∿60 MeV. This covers the expected energy-loss range from minimum-ionizing, singly charged particles to just above the value for minimum-ionizing magnesium nuclei. The fused silica of D3' has an index of refraction of about 1.6 in the near ultraviolet, dropping to about 1.45 in the visible. This corresponds to a Čerenkov threshold of about 300 MeV/nucleon.

The calculated response of the detectors to particles of various charges and energies is shown in Figure II-2. Here energy loss is calculated from (*Evans*, 1955)

$$dE/dx = \frac{4\pi e^4 Z^2 N Z_a}{m_e V^2} [\ln(2m_e V^2/I) - \ln(1 - \beta^2) - \beta^2] \qquad \text{(II-1)}$$

where Z is the charge of the incident particle, $V = \beta c$ is its velocity, Z_a is the charge of the absorbing material (Z_a = 14 for silicon), m_e is the mass of the electron, N is the number of absorber atoms per cm^3, and I is an empirical "excitation potential" whose value for silicon is ∿170 eV. For silicon, this can be rewritten

$$dE/dx = (.359 \text{ MeV/cm}) (Z^2/\beta^2) [8.70 + \ln(\beta^2\gamma^2) - \beta^2] \qquad \text{(II-2)}$$

Figure II-1

Cross-sectional view of OGO-6 Čerenkov Telescope.

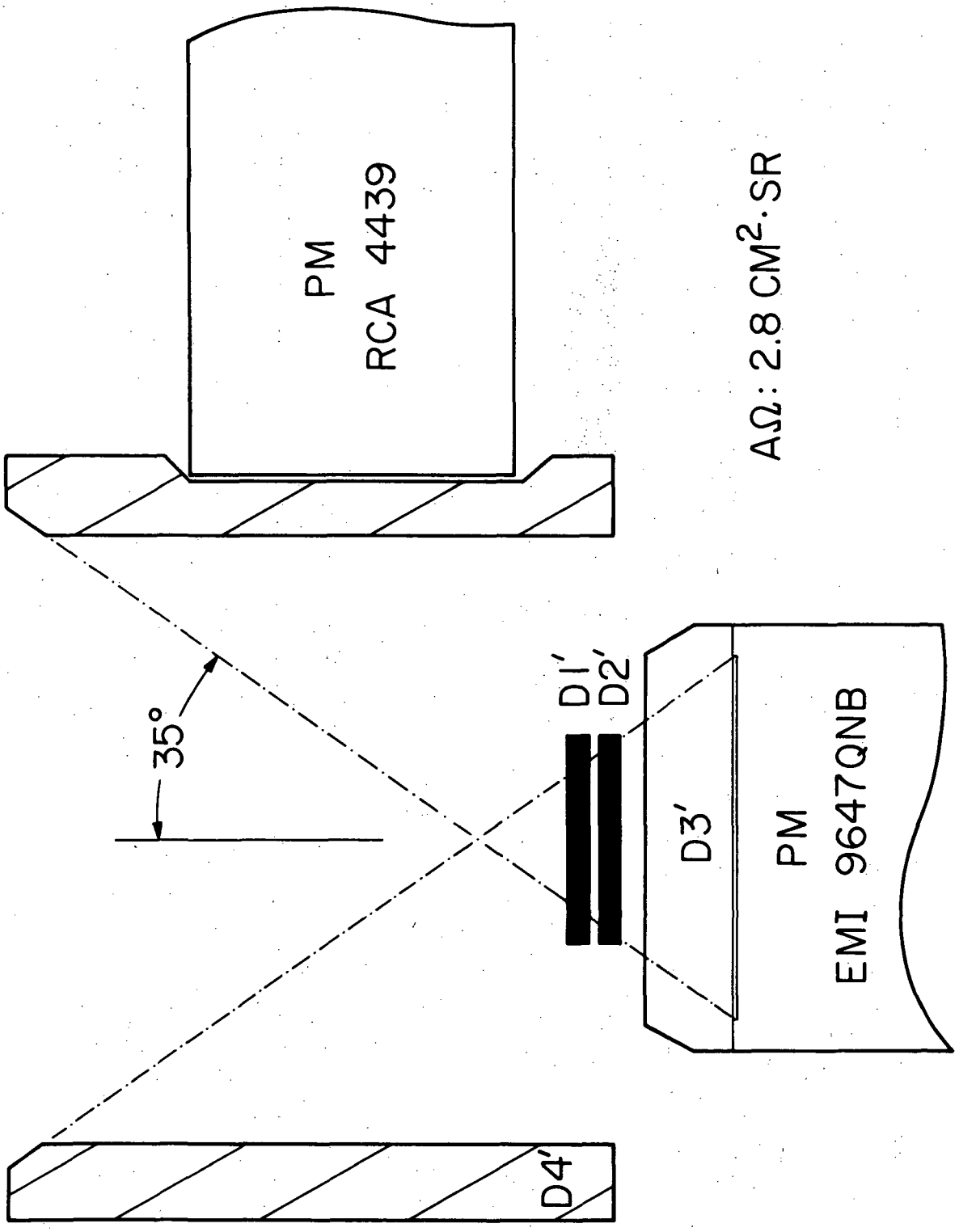

Figure II-1

Figure II-2

Predicted response of OGO-6 Čerenkov Telescope. Čerenkov light output is normalized so a singly charged, fully relativistic particle gives unit light output. Calculated using a value of 1.58 for index of refraction.

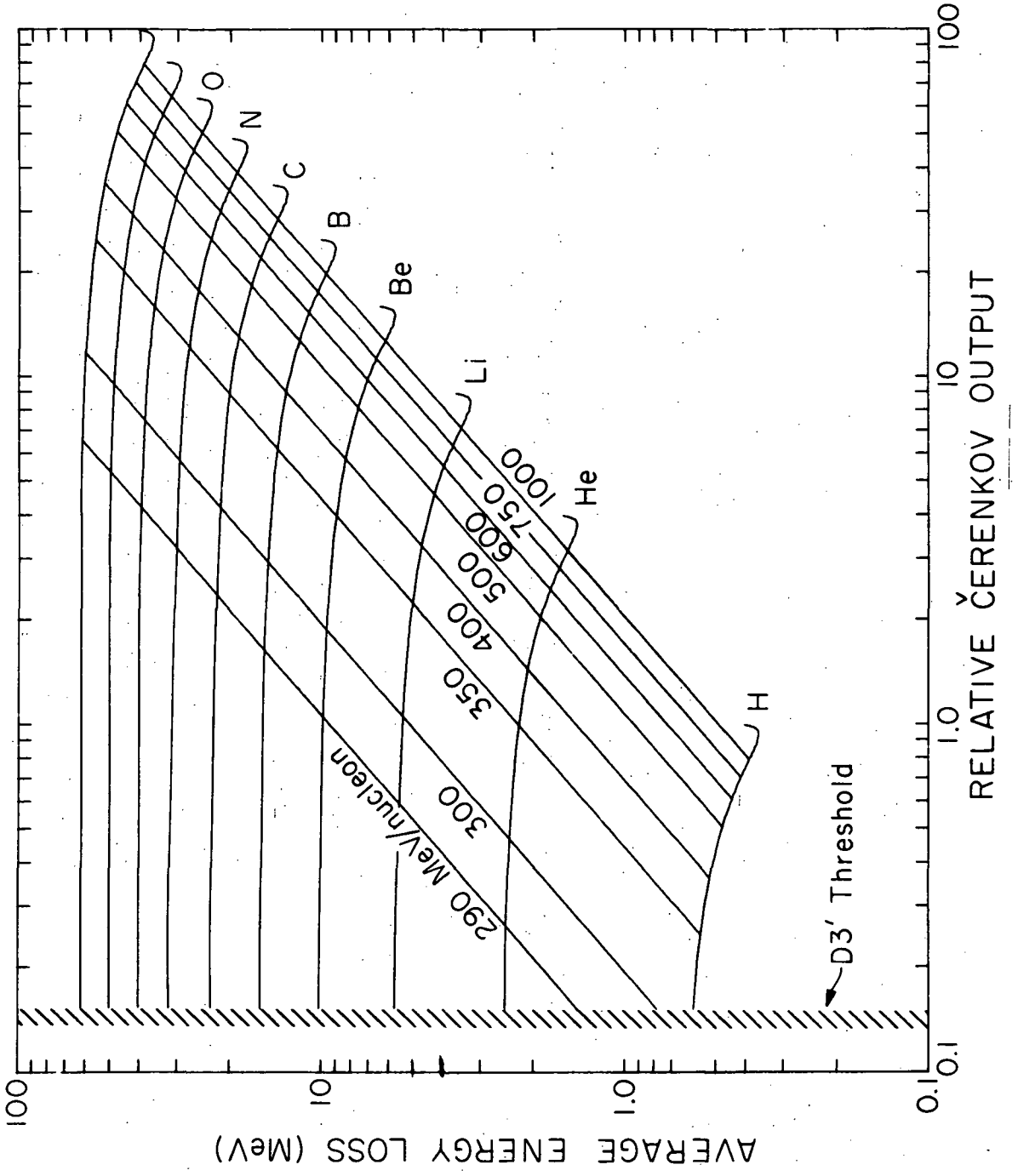
AVERAGE ENERGY LOSS (MeV)
100
10
1.0
0.1
RELATIVE ČERENKOV OUTPUT
0.1
1.0
10
100
O
N
C
B
Be
Li
He
H
1000
750
600
500
400
350
300
290 MeV/nucleon
D3′ Threshold

Figure II-2

where γ is the Lorentz factor.

Čerenkov output is calculated from (*Evans*, 1955)

$$d^2N/dxd\nu = 2\pi\alpha Z^2c^{-1}\left(1 - \frac{1}{\beta^2n^2(\nu)}\right) \qquad \text{(II-3)}$$

where $d^2N/dxd\nu$ is the number of photons emitted per unit path length in the frequency interval ν to $\nu + d\nu$, $\alpha = 1/137$, and $n(\nu)$ is the index of refraction of the material. If we include the response of the photomultiplier tube as $\varepsilon(\nu)$ = number of photoelectrons/photon, then

$$K = 2\pi\alpha Z^2c^{-1}\Delta x \int [1 - \beta^{-2}n^{-2}(\nu)]\ \varepsilon(\nu)d\nu \qquad \text{(II-4)}$$

where the integration is done over all frequencies for which the integrand is greater than zero, and K is the total number of photoelectrons emitted from the photocathode. A reasonably good approximation for the OGO-6 photomultiplier is $\varepsilon \simeq .18$ for vacuum wavelengths from $\sim$170 nm to $\sim$520 nm and zero elsewhere, and $n \simeq 1.58$ in this range. Using $\Delta x = 1$ cm, we get

$$K \simeq 345\ (1 - .40/\beta^2)Z^2 \text{ photoelectrons} \qquad \text{(II-5)}$$

for normally incident particles of charge Z. For fully relativistic ($\beta = 1$), downward-moving particles, this is $K \simeq 200Z^2$ photoelectrons. The face of the silica window is painted black to discriminate against upward-moving particles (*Wenzel*, 1968).

C. Calibrations

Three types of calibrations are available to assist in the interpretation of data from this experiment. Electronic calibrations on the ground provide detailed information on pulse-height analyzer (PHA) linearity, temperature sensitivity, and stability. Calibrations using artificially accelerated protons (Caltech Tandem Van de Graaff) and electrons (Caltech Synchrotron), and natural muons, alphas, and β-particles yield information on detector diameters, thicknesses, and uniformities. These calibrations are described in detail elsewhere (*Murray*, 1971). The electronic calibrations are summarized here to illustrate the correspondence between detector outputs and PHA channels. Figure II-3 shows the 25°C calibrations for D1' and D2', and Figure II-4 shows the same for D3'.

This experiment was designed with two identical dE/dx detectors in order to minimize the effects of statistical fluctuations in the energy-loss process (*Symon*, 1948), and to reduce background from a number of sources. However, the overall responses of the two detectors (including amplifiers and PHA's) are not exactly identical, as can be seen from the calibrations shown in Figure II-3. These calibrations were confirmed by using the relativistic particle peaks for D1' and D2', in a manner similar to that indicated below. In order to compare the two detectors, a correction was made to the D1' response by defining

$$D1'' = D1' + .075\ (D1' - 190) \qquad \text{(II-6)}$$

Figure II-3

Laboratory calibration of D1' and D2' at 25°C. Piecewise-linear transfer characteristic, explained in Althouse *et al.* (1967), is used to achieve large dynamic range without sacrificing resolution at low signal levels.

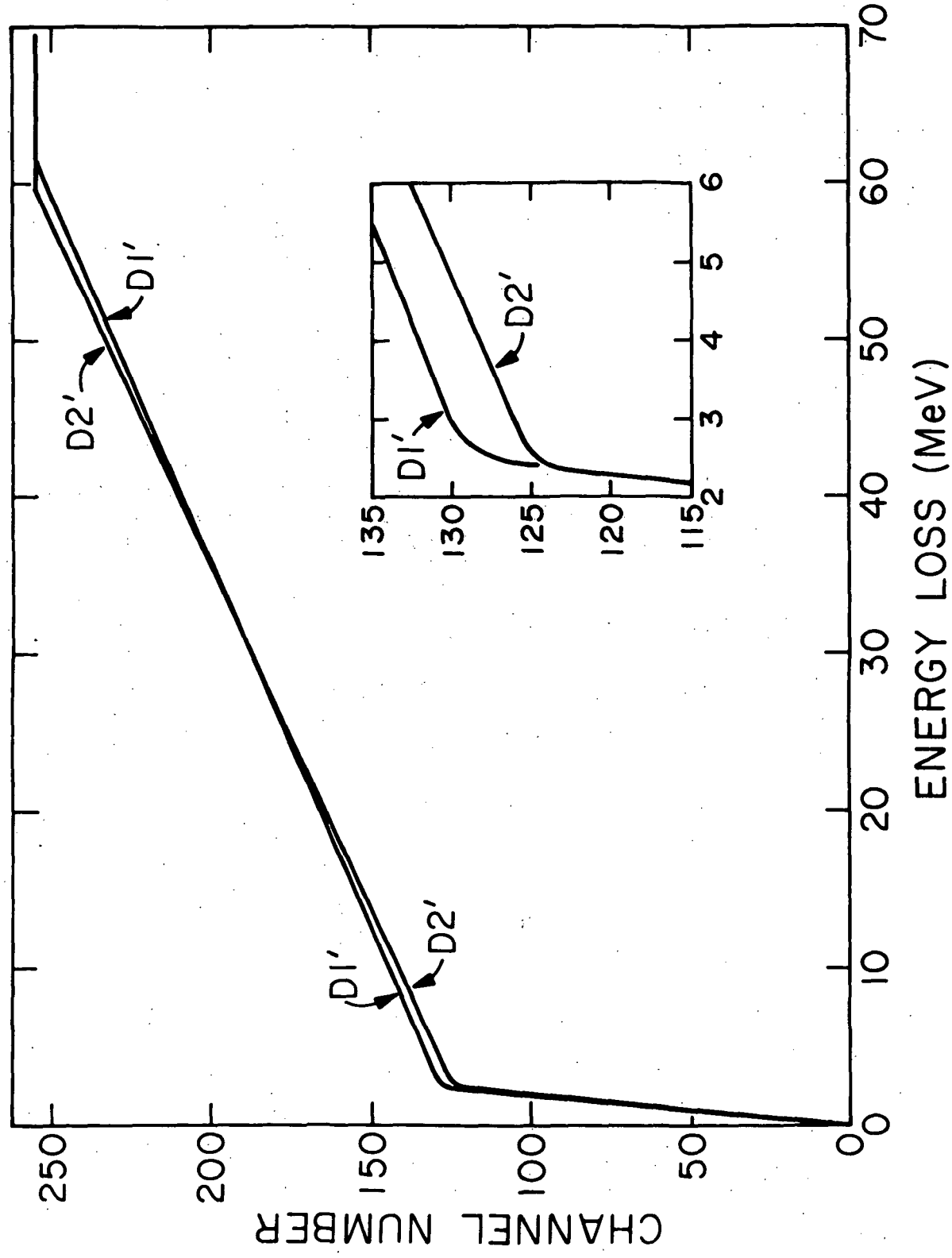
CHANNEL NUMBER
ENERGY LOSS (MeV)
D1′
D2′
D1′
D2′
D1′
D2′
0
50
100
150
200
250
0
10
20
30
40
50
60
70
115
120
125
130
135
2
3
4
5
6

Figure II-3

Figure II-4

Laboratory calibration of D3' at 25°C. PHU (Pulse Height Unit) is a calibrating unit corresponding to a photomultiplier output of about 25 picocoulombs. One picocoulomb corresponds to a relative light output of about unity in Figure II-2.

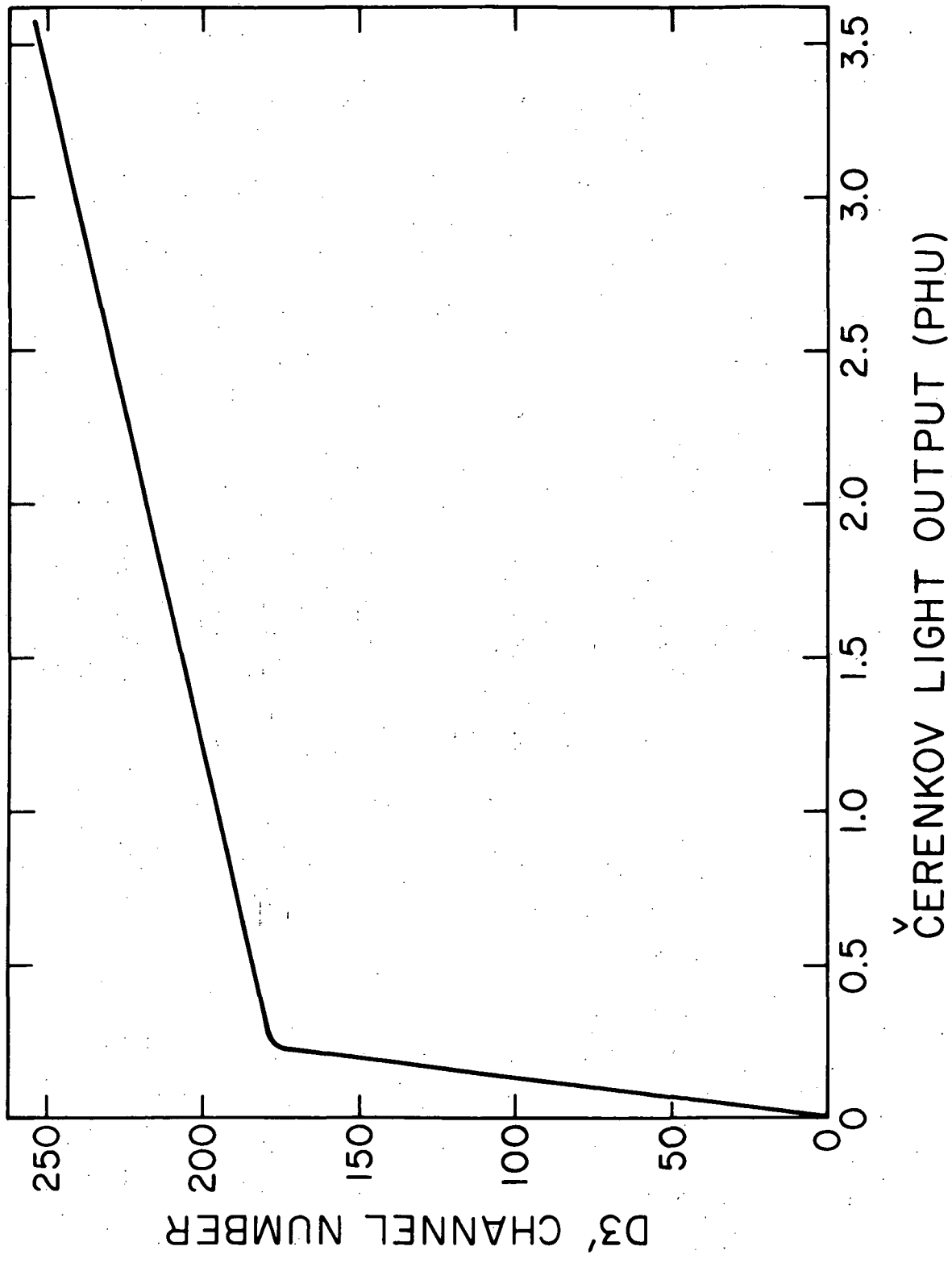
D3' CHANNEL NUMBER
250
200
150
100
50
0
0
0.5
1.0
1.5
2.0
2.5
3.0
3.5
ČERENKOV LIGHT OUTPUT (PHU)

Figure II-4

for D1' > 127. For D1' = 125 to 127, D1" = 125. The validity of this correction was checked by examining the means of the D1" - D2' distributions as discussed in Chapter III.

The most important calibration is provided by actual flight data accumulated at locations where the vertical geomagnetic cutoff rigidity (P_c) was sufficiently high ($\gtrsim$ 6.4 GV) to ensure that only particles having $\beta \simeq 1$ entered the detector telescope. Note from equations (II-2) and (II-5) that, for a fixed value of β, both energy-loss and Čerenkov outputs are linear in Z^2. Therefore, we expect particles having $\beta \simeq 1$ to produce data points clustered along a line with $\Delta E \propto \check{C} \propto Z^2$. Figure II-5 illustrates the distribution in (D1" + D2')/2 *versus* D3' space of $\beta \simeq 1$ events selected according to consistency criteria discussed in a later section. Since the individual charge peaks are clearly separated, it is a simple matter to count up the number of events of a given charge, as a function of either ΔE channel or $\check{C}$ channel. While this procedure is subject to some error in charge assignment for events far from the peaks, the error is not large, and in any case is not important for the present purpose of determining the locations of the peaks. A more sophisticated charge determination technique is discussed in Chapter III.

The results of this procedure for the boron and nitrogen peaks are shown in Figure II-6. Similar plots were made for all the peaks, and the results for $3 \leq Z \leq 10$ are shown in Figure II-7. As expected, we have $\Delta E \propto Z^2$ and $\check{C} \propto Z^2$. The lines fitted to the peak positions form the basic calibration of the instrument. This calibration may be expected to be

Figure II-5

Scatter plot of high-rigidity events showing positions of peaks for relativistic particles. Sample includes only events with $P_c \geq 6.4$ GV to ensure that only particles having $\beta \simeq 1$ contribute to the distributions. Vertical axis represents average of two energy-loss measurements; horizontal axis is Čerenkov output. Numbers on plot represent number of events. Letter code is logarithmic, with each letter representing a factor of $10^{0.1}$, i.e., A ≃ 10, F ≃ 32, K ≃ 100, etc. Events selected as discussed in Chapter III. Light lines delimit preliminary charge assignment used only for determination of locations of peaks.

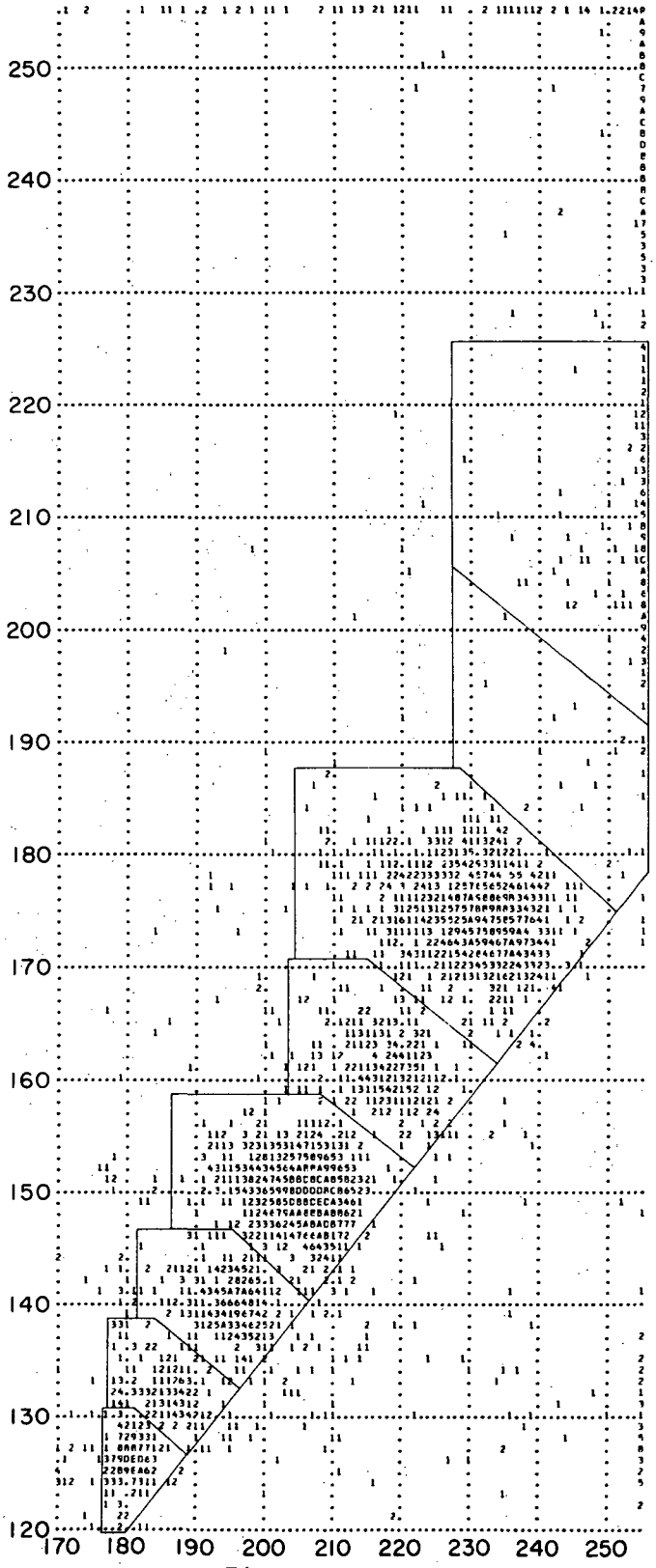
250
240
230
220
210
200
190
180
170
160
150
140
130
120
170 180 190 200 210 220 230 240 250

Figure II-5

Figure II-6

Events selected from boron and nitrogen distributions of Figure II-5. Accurate charge identification was not attempted for these plots, the purpose of which is to locate the centers of the distributions.

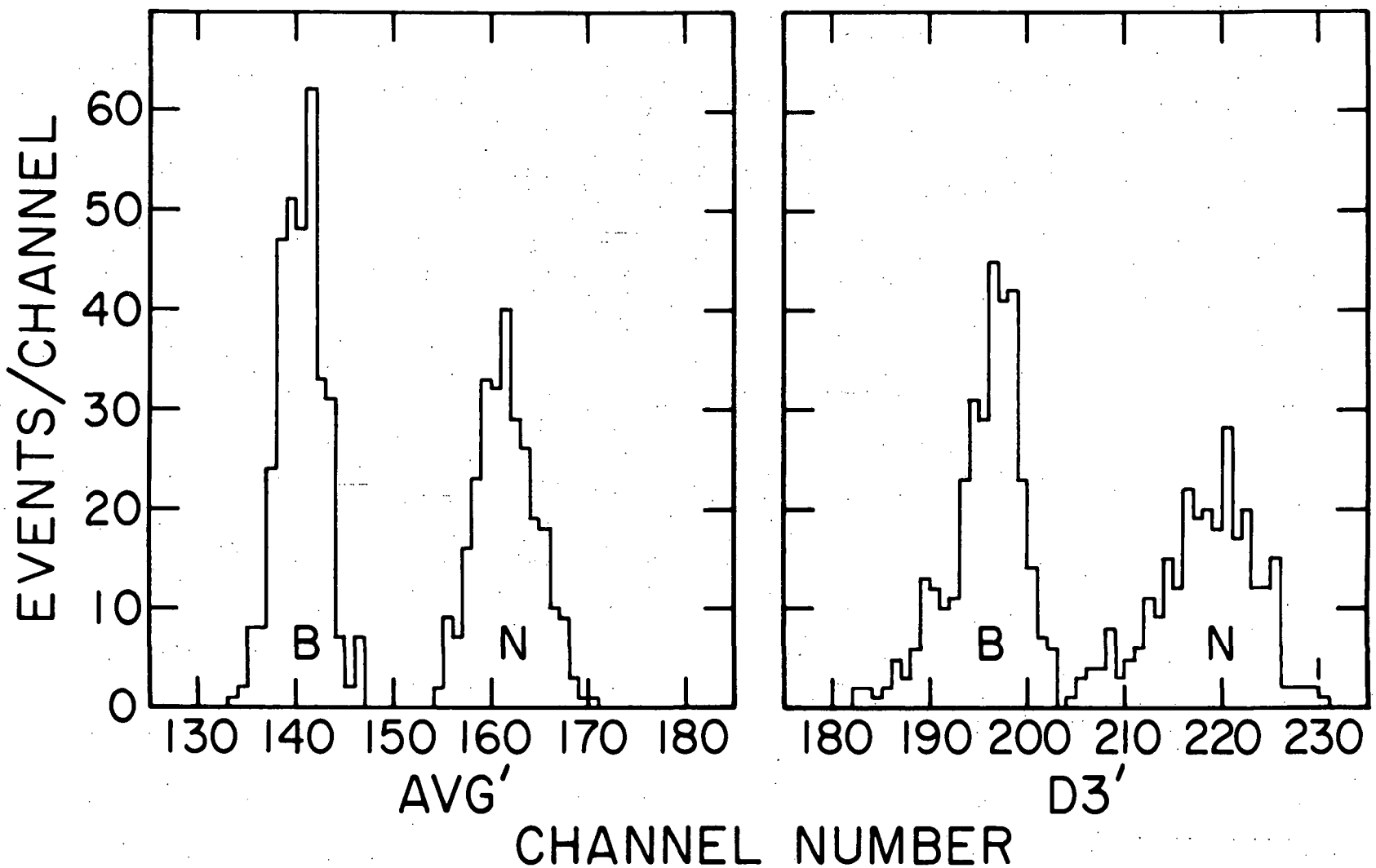
EVENTS/CHANNEL
60
50
40
30
20
10
0
B
N
130 140 150 160 170 180
AVG′
B
N
180 190 200 210 220 230
D3′
CHANNEL NUMBER

Figure II-6

Figure II-7

Peak positions of distribution shown in Figure II-5, obtained from plots such as those in Figure II-6. Uncertainties in locations of peaks are ≤ 0.2 channel for $Z \leq 8$. Poor statistics make locations more uncertain for $Z > 8$.

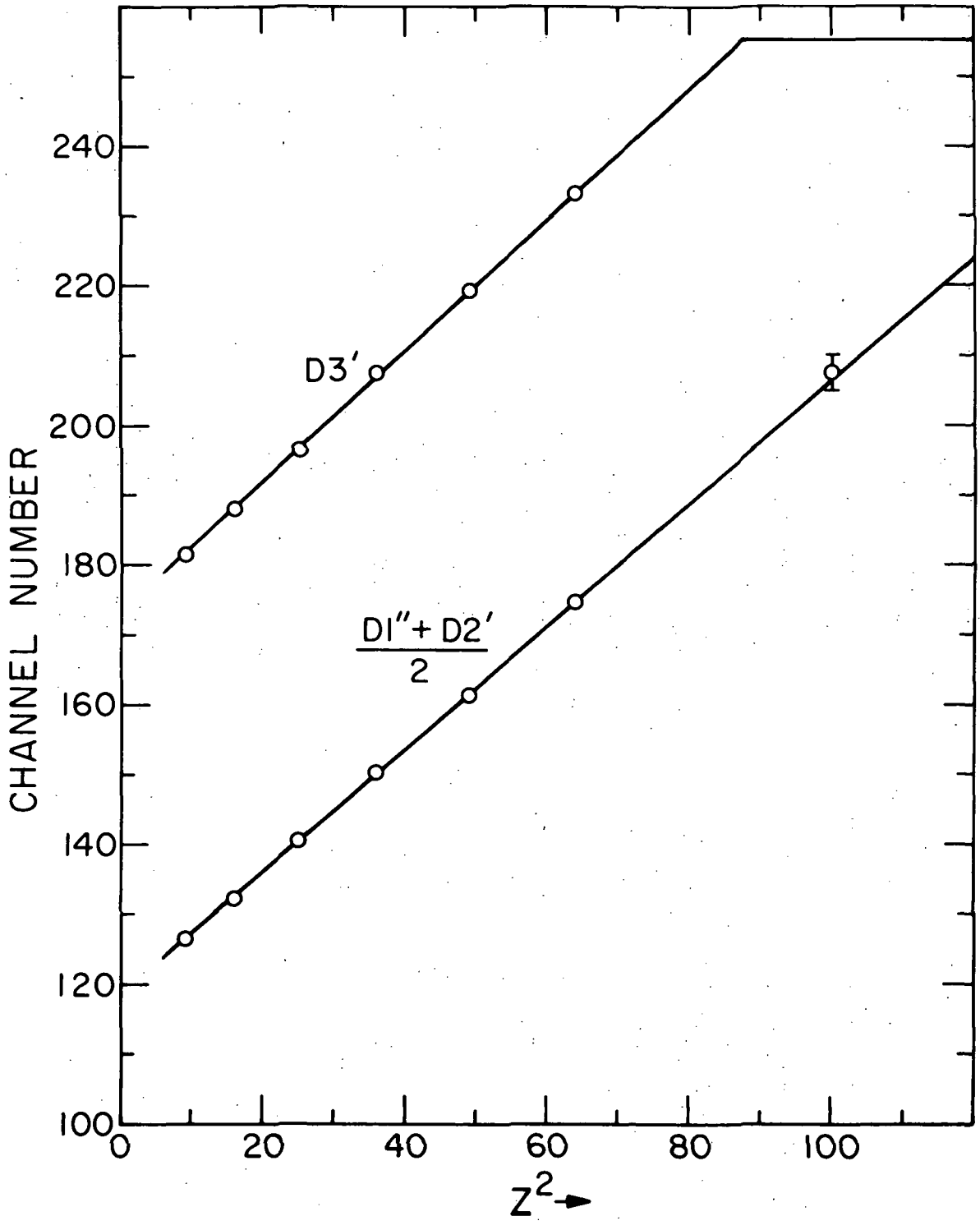
CHANNEL NUMBER
240
220
200
180
160
140
120
100
0
20
40
60
80
100
Z^2
D3′
$\frac{D1'' + D2'}{2}$

Figure II-7

temperature sensitive, due to variations of the characteristics of the electronics with temperature. However, the temperature of the spacecraft -Z door, on which the experiment is mounted, was held at 21.3 ± 1.9°C by the spacecraft Thermal Control System. Comparison of data taken when the temperature was ≤20°C and ≥23°C indicate a shift of ≤1/2 channel in the position of the oxygen peak (Figure II-7), so all data discussed in this thesis were combined without regard to temperature.

III. Data

A. Event Selection Criteria

In order to take advantage of the redundant energy-loss measurements provided by D1' and D2', we need to understand the details of the overall response functions of the detector systems. The energy-loss distributions in D1' and D2' are highly asymmetrical for particles with Z = 1 or 2. These distributions have been discussed by Symon (*Symon*, 1948). However, for Z > 2, the distributions are more nearly Gaussian. The asymmetry of the distributions arises from statistical fluctuations of the relatively small number of collisions in which the energy transfer is comparable to the average energy loss. The average energy loss is proportional to Z^2, while the maximum energy transferrable to an electron in a single collision is a function only of the velocity of the incident particle:

$$E_{e,max} = 2m_e c^2 \beta^2/(1 - \beta^2) \qquad \text{(III-1)}$$

hence independent of Z. The fluctuations due to these few high energy collisions therefore become less important with increasing charge. In addition, variations in detector thickness and particle incidence angles, and electronic noise in the amplifiers, tend to broaden the distributions.

A sample of the D1' *versus* D2' distribution for boron and carbon having $\beta \simeq 1$ is shown in Figure III-1. Since D1' (or D1") and D2' are nearly identical, they show similar distributions, and can thus be

Figure III-1a

D1' *versus* D2' for events having $P_c \geq 6.4$ GV, with $194 \leq D3' \leq 203$, showing most of boron distribution and part of carbon. Most of events not part of main distributions are assumed to have suffered detector edge effects, as discussed in text. Diagonal lines, representing constant D1" + D2', are used for approximate charge assignment for Figure III-2.

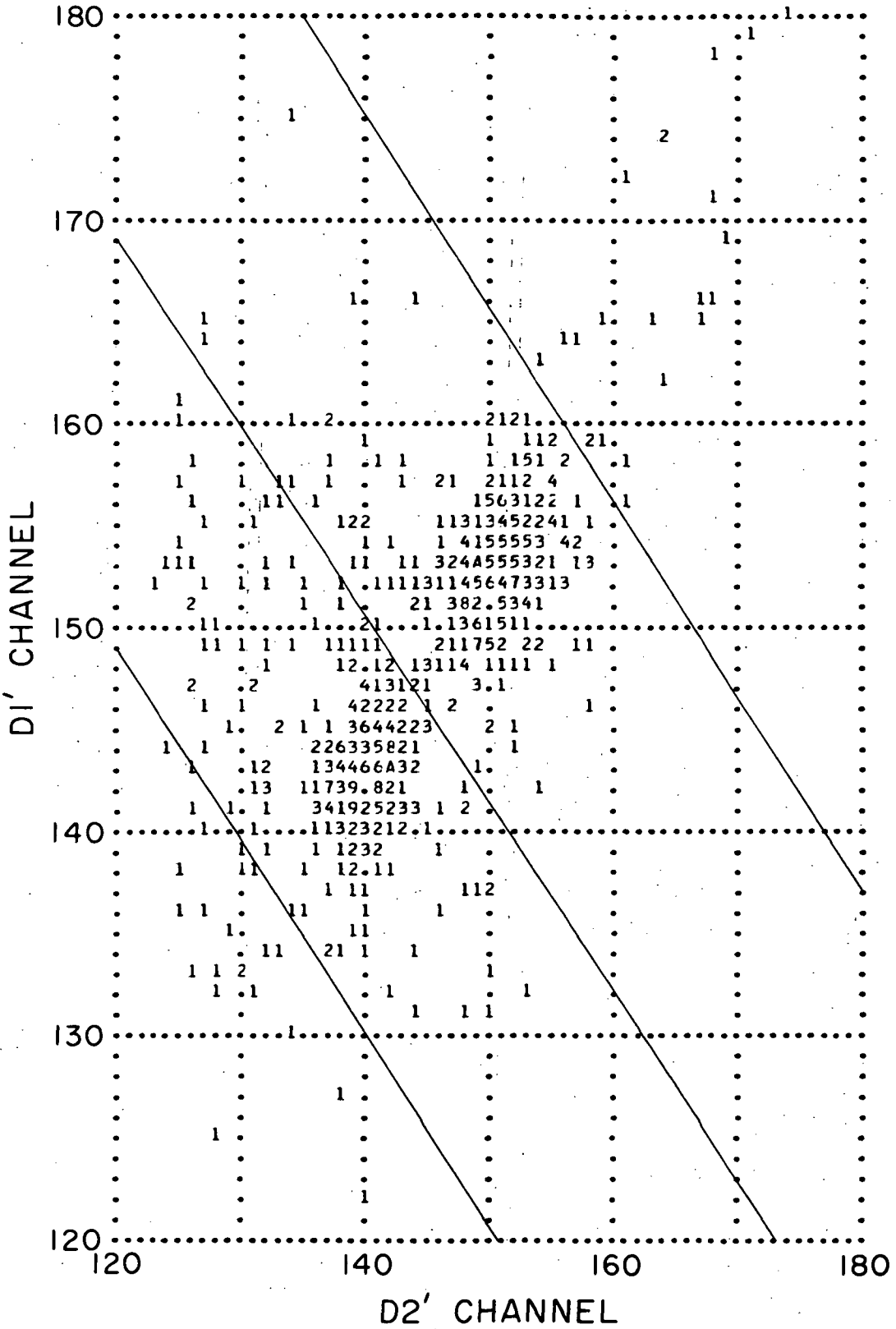

Figure III-1a

Figure III-1b

D1' *versus* D2' for events having $P_c \geq 6.4$ GV, with $204 \leq D3' \leq 214$, emphasizing carbon distribution and showing some nitrogen and oxygen. Otherwise similar to Figure III-1a.

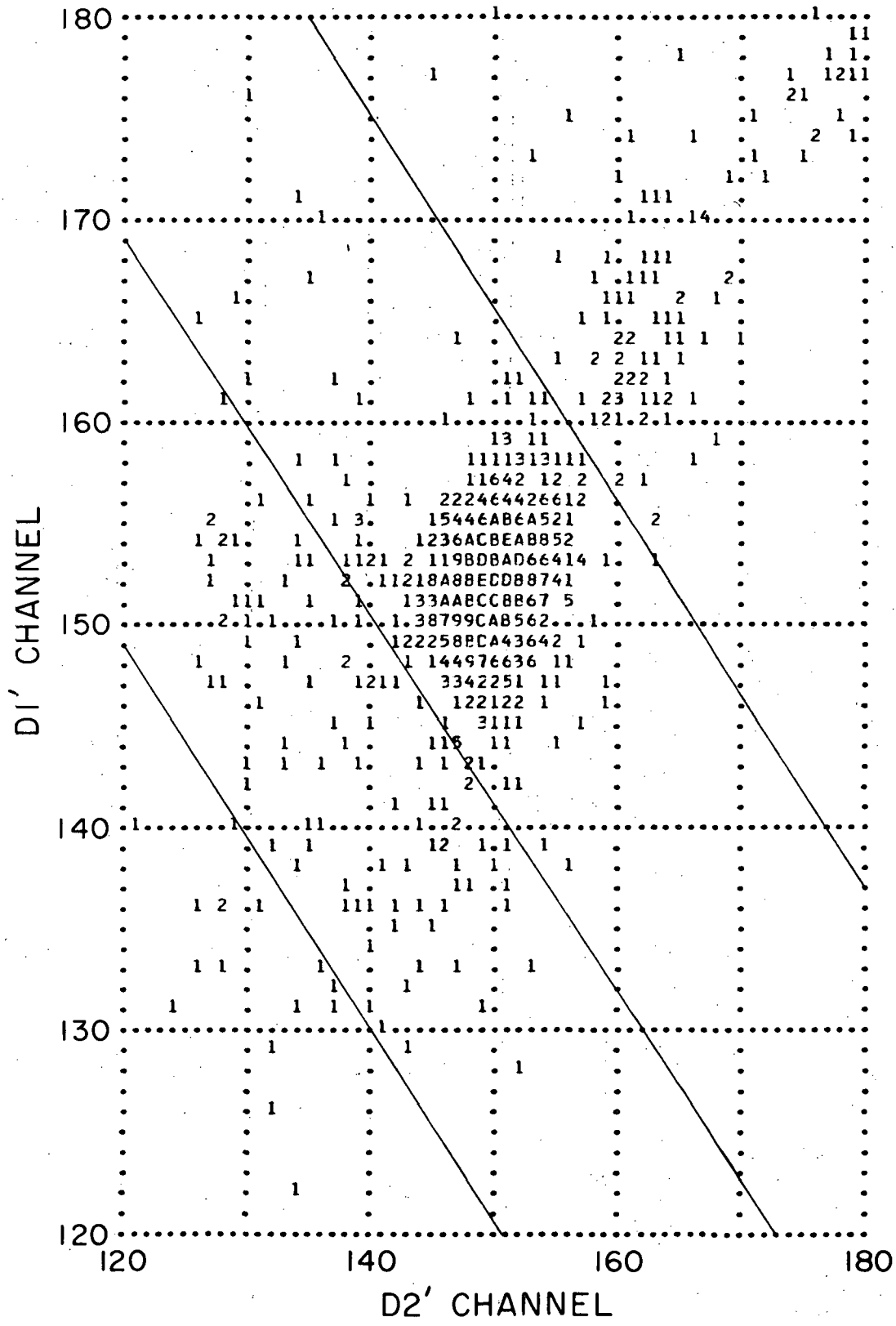

Figure III-1b

combined directly in a number of ways. Figure III-2 shows some of the distributions of the difference D1"-D2' for various charges. For this purpose, the charges were assigned simply by selecting intervals of D1"+D2' as implied by Figure III-1, and do not represent a rigorous charge identification. These distributions are centered at zero (±0.4), confirming the validity of Equation II-6. Notice that the central parts of the distributions are essentially Gaussian, but there are significant numbers of events with D1"-D2' too large. These may occur through two mechanisms: nuclear interactions in the detectors, and edge effects.

Calculations using geometrical cross sections indicate that ∿1.3% (lithium) to ∿1.9% (magnesium) of incident nuclei will suffer nuclear interactions in D1' or D2'. Some of these will be rejected because they trigger D4'. The others will have some degree of inconsistency between their D1" and D2' pulse heights, which shows up as extra events in the wings of the distributions shown in Figure III-2, or as events far from the peaks in Figure III-1.

A much more important source of this background is edge effects in D1' and D2'. This problem arises from non-uniformity in the electric field near the edges of the detectors, causing incomplete collection of electron-hole pairs formed by the incident particle. Thus, a particle which passes through the edge of D1', and then closer to the centers of D2' and D3', will leave a normal signal in D2' and D3', but the D1' signal may be anywhere between zero and the normal value. Likewise, a particle may leave a normal signal in D1', pass through the edge of D2', and then still leave a normal signal in D3', since D3' is much larger in

Figure III-2

Distributions of difference D1"-D2' for elements lithium through carbon. Charge assignments were made by selecting contiguous intervals in D1" + D2', and are not intended to be precise.

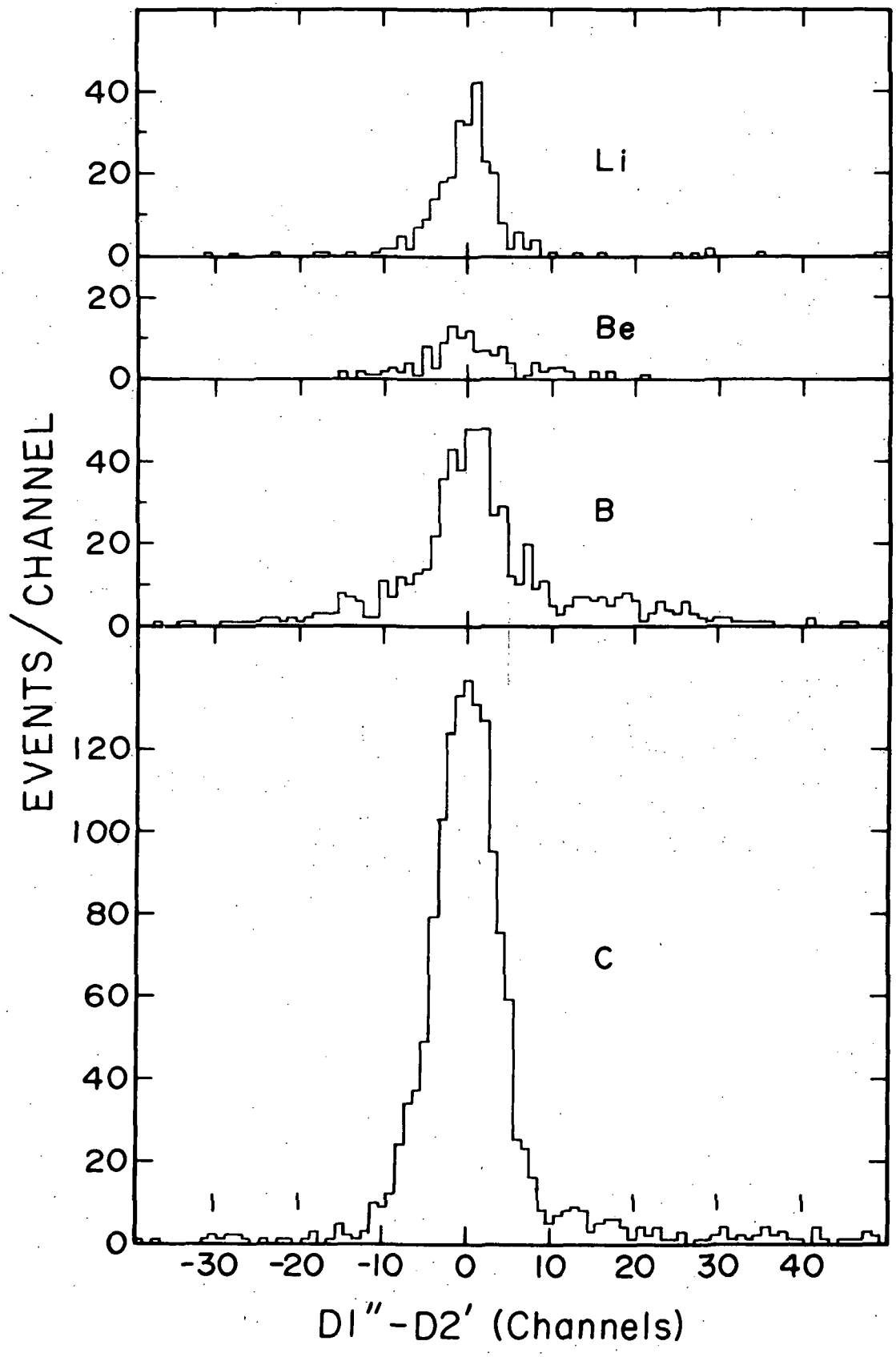
EVENTS / CHANNEL
Li
Be
B
C
0
20
40
60
80
100
120
-30
-20
-10
0
10
20
30
40
D1″-D2′ (Channels)

diameter than D2'. The geometrical factor for the latter process ($\sim$0.34 cm^2sr) is substantially larger than for the former ($\sim$0.15 cm^2sr). This is borne out by examination of Figure III-2. The large number of events in the wings of the "boron" distribution are due to carbon nuclei which passed through the edge of D1' or D2'. This can be seen in Figure III-1 as events extending towards low D1' or D2' from the carbon peak. It is apparent that there are more events with low D2' (high D1"-D2') than *vice versa*. Since this is purely a geometrical effect, we do not affect the elemental abundance ratios by ignoring these events, and the absolute fluxes will be correct if the geometry is calculated correctly.

In order to reject the maximum number of background events while retaining most of the good events, we need an accurate estimate of the shape of the D1"-D2' distributions. To obtain this, we selected the central portions of the distributions, *i.e.*, $|D1''-D2'| \leq 10$, and plotted them on probability paper. The results are shown in Figure III-3. These plots indicate that the centers of the distributions can be represented by Gaussians, and the widths of the Gaussians can be determined fairly accurately. Widths read directly from Figure III-3 are shown in Figure III-4.

We expect these widths to be composed of a part proportional to Z, due to the fluctuations in energy loss, and a part independent of Z, due to electronic noise. Thus we should have

$$\sigma^2 = \sigma_A^2 + \sigma_B^2 Z^2 \ . \qquad \text{(III-2)}$$

Figure III-3

Integrals of D1"-D2' distributions for $|D1"-D2'| \leq 10$ plotted on probability paper for purpose of determining widths of distributions.

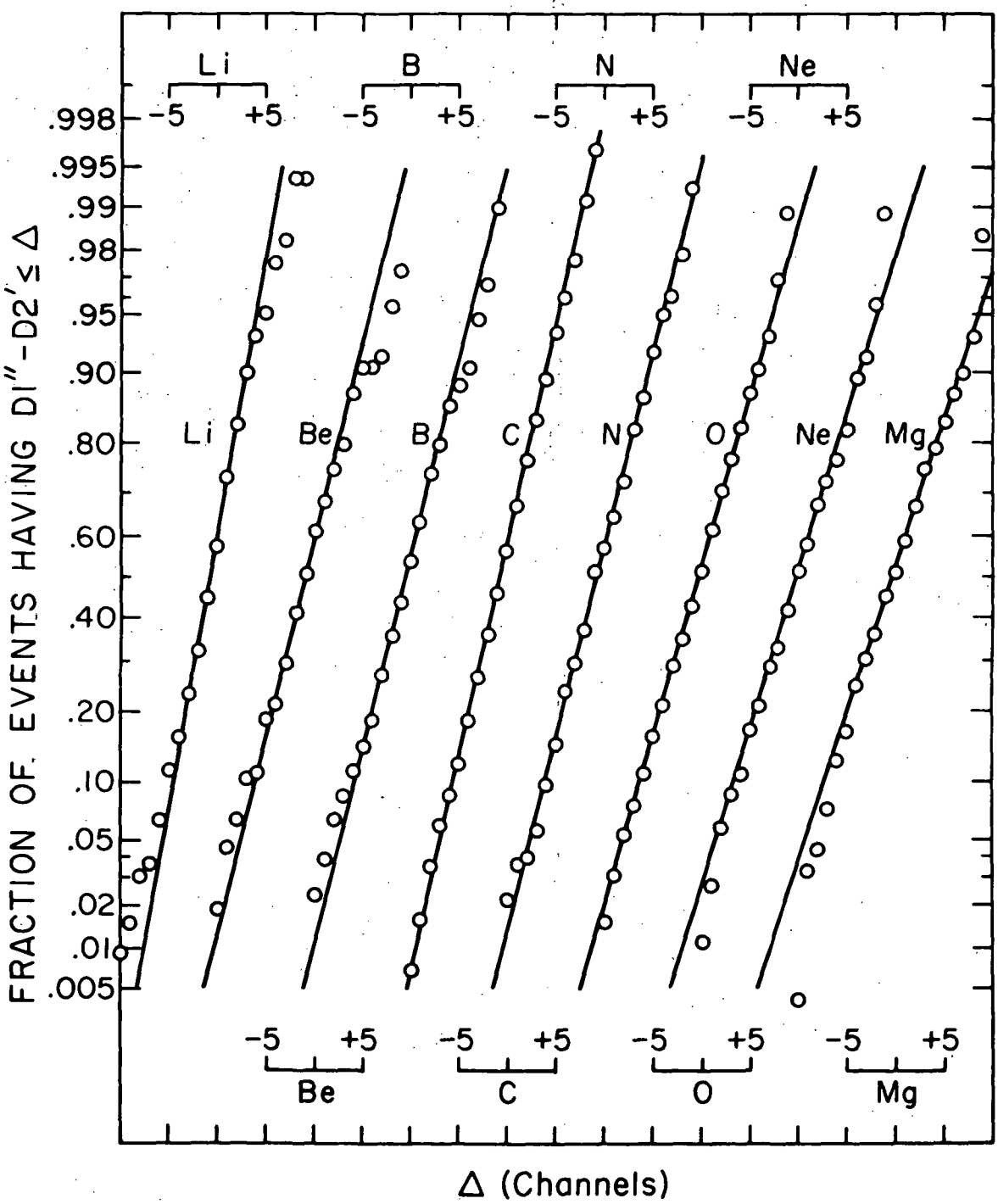
Li
B
N
Ne
-5
+5
.998
.995
.99
.98
.95
.90
.80
.60
.40
.20
.10
.05
.02
.01
.005
FRACTION OF EVENTS HAVING DI''-D2' ≤ Δ
Li
Be
B
C
N
O
Ne
Mg
Be
C
O
Mg
Δ (Channels)

Figure III-3

Figure III-4

Widths (σ) of Gaussian distributions of D1"-D2' obtained from Figure III-3. The dashed line is a weighted least-squares fit to Equation (III-2). The solid line is the approximation used for event selection.

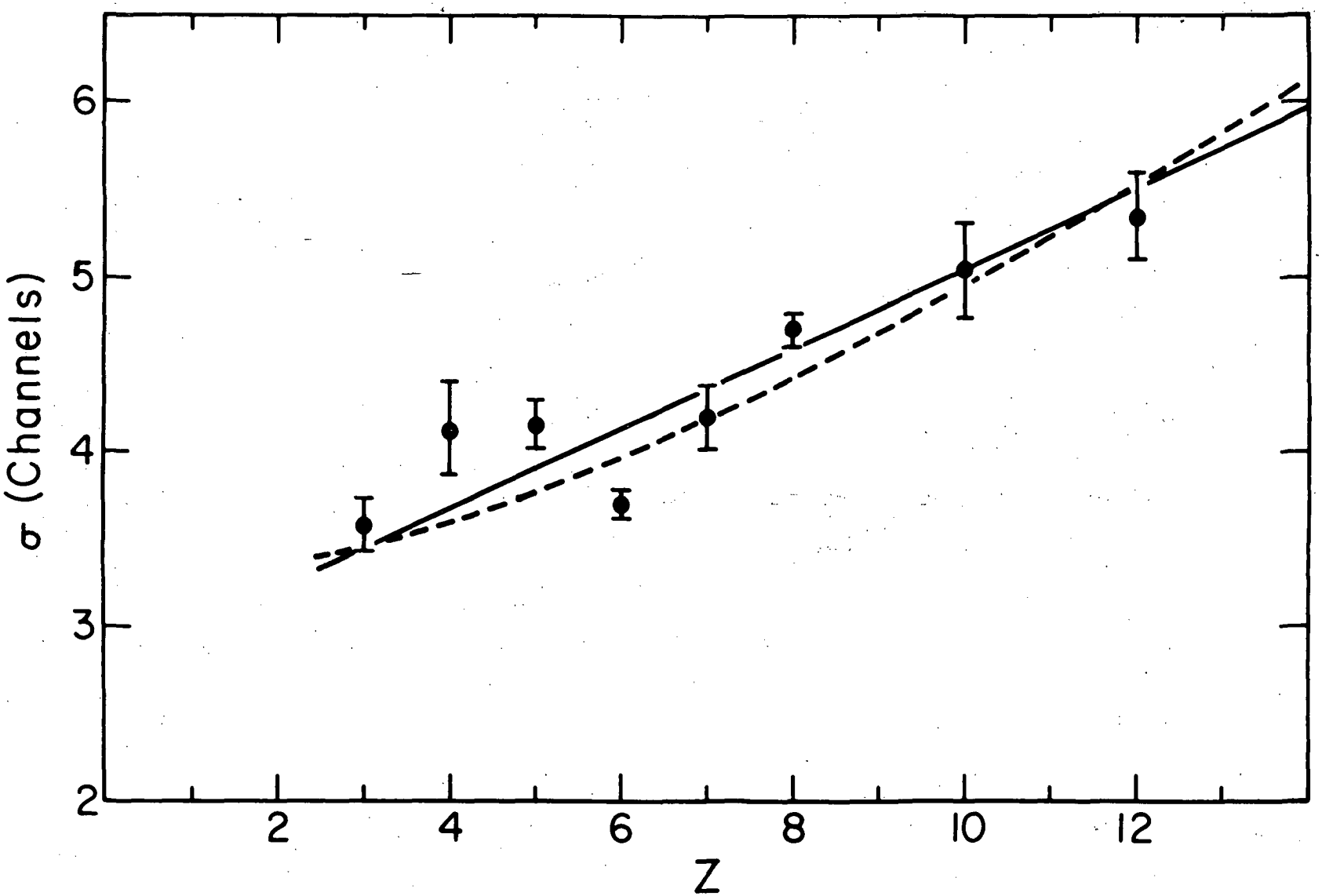
σ (Channels)
6
5
4
3
2
2
4
6
8
10
12
Z

A weighted least-squares fit of this function to the observed values is shown as the dashed line in Figure III-4. The solid line is an approximation of the form

$$\sigma = \sigma_0 + \sigma_1 Z \qquad \text{(III-3)}$$

which appears to fit equally well. The difference between (III-2) and (III-3) is smaller than the uncertainties of the points in Figure III-4, and is not significant in any case, as discussed below.

Figure III-2 indicates that the bulk of the good events have $|D1''-D2'| \lesssim 10$. Using this as a guide, we chose a tolerance of 2.5σ in the D1"-D2' distributions as an event selection criterion. Using Figure II-7 to relate Z to D1"+D2', and obtaining σ from the straight line in Figure III-4, we require

$$|D1''-D2'| \lesssim 7.375 + \sqrt{.186\ (D1''+D2'-236)}\ , \qquad \text{(III-4)}$$

i.e., $|D1''-D2'| \lesssim 2.5\sigma$. At this tolerance, we reject only 1.24% (nominally) of the events in a Gaussian distribution. Assuming that the correct σ values are the points plotted in Figure III-4 rather than the dashed line, the rejection varies from 0.5% to 1.9%. Therefore, we claim that the event selection process is nearly independent of charge, and that systematic errors in the elemental abundance ratios from this source are at the <1% level.

Events which are outside the 2.5σ tolerance are about 19% of the total. As discussed above, most of these are the result of detector edge effects, and can be accounted for geometrically, independent of charge. Using geometrical cross-sections, we expect nuclear interactions in D1' and D2', which have a weak charge dependence, to affect 1% to 2% of the total events. Rejection of nearly all of these by (III-4), introduces a weakly charge-dependent, systematic error at the 1% level. Since statistical errors we will be discussing later are $\sim$5%, we feel safe in neglecting the above-mentioned errors in the subsequent discussion.

A small fraction of events have similar pulse heights after passing through the edges of <u>both</u> D1' and D2'. The geometrical factor for this is about 0.16 cm^2sr. Those falling below the diagonal line in Figure II-5 are rejected.

B. Charge, Velocity Assignment

Equations (II-2) and (II-5), combined with calibrations derived from Figures II-3, II-4, and II-7, predict average pulse heights for particles with given charge and velocity. An example of this is shown in Figure III-5. Here, data taken at cutoff rigidities below 1.8 GV are compared with the expected average positions for each charge and velocity in an AVG' *versus* D3' matrix (the term AVG' refers to the average of D1" and D2' channel numbers for each event). Events having D3' < 179 were moved to the interval 173 ≤ D3' < 179, using the calibration shown in Figure II-4. This effectively produces a linear response for the entire range of pulse heights, at the expense of losing resolution for Z < 3.

The pair of equations (II-2) and (II-5) can be solved for charge and velocity, given the appropriate pulse heights and calibrations. If we allow fractional charges, to account for statistical fluctuations, we can assign a unique charge and velocity to each (AVG', D3') pair. However, since each channel has a finite width, the following procedure was used. Each (AVG', D3') pair was considered a rectangle, containing a certain number of events. Lines of constant charge were laid across this rectangle, and the events were assigned to various charge bins in proportion to the area assignable to each bin. Events which, due to statistical fluctuations, lie in channels beyond the $\beta \simeq 1$ line shown in Figure III-5, are moved first to the $\beta \simeq 1$ line in a direction related to the ratio of the widths of the AVG' and D3' distributions. Events were accumulated in bins 0.1 charge unit wide. Results of applying this procedure to the data in Figure III-5 are shown in

Figure III-5

Scatter plot of events recorded at $P_c < 1.8$ GV, otherwise similar to Figure II-5. Calculated average response for each charge is indicated by solid lines. Diagonal line is fit to peaks shown in Figure II-5. Step-shaped line delimits events rejected for AVG' *versus* D3' inconsistency as discussed in text.

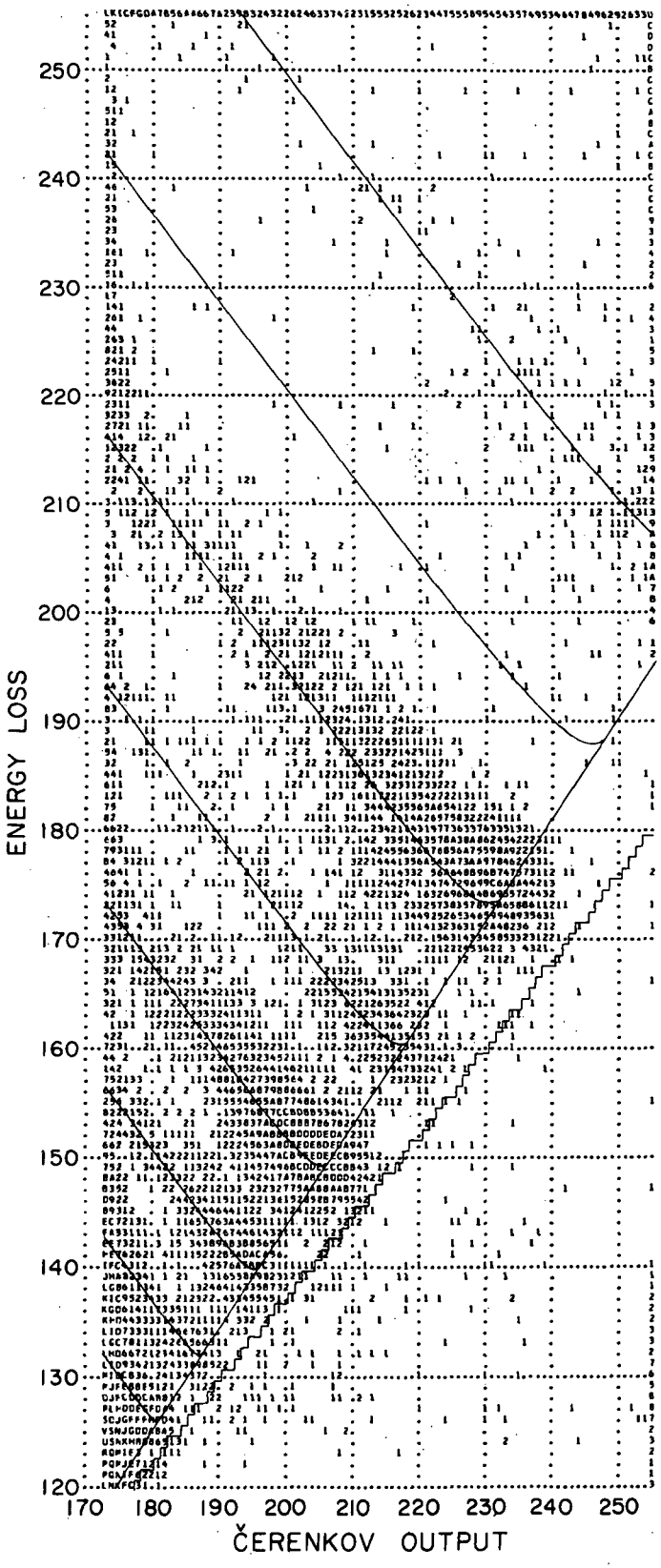
ENERGY LOSS
250
240
230
220
210
200
190
180
170
160
150
140
130
120
170 180 190 200 210 220 230 240 250
ČERENKOV OUTPUT

Figure III-6. Similar results for data collected at cutoff rigidities above 1.8 GV are shown in Figure III-7.

These distributions are fit quite well by a sum of Gaussians:

$$N(z) = \sum_{j=3}^{9} A_j \exp\left[(z - z_j)^2/2\sigma_j^2\right] + r(s - z) \qquad \text{(III-5)}$$

for $2.5 \leq z \leq 9.3$. Here z is a continuous variable which represents charge. The last term is used to account for the small helium background under the lithium peak. The parameter r is a constant for $z < s$, and zero for $z > s$. In order to allow for possible inaccuracy in detector calibrations, z_j was allowed to vary quadratically:

$$z_j = aj + b + gj^2 \qquad \text{(III-6)}$$

Likewise,

$$\sigma_j = cj + d + hj^2 \qquad \text{(III-7)}$$

In all the fits, a, b, c, d, g, h, r, s, and the A_j were free parameters. As might be expected from looking at Figures III-6 and III-7, the results were always $a \simeq 1$, $b \simeq c \simeq g \simeq h \simeq 0$, and $d \simeq 0.2$; *i.e.*, the charge resolution was about 0.2 charge unit, nearly independent of charge. Results for each fit are shown in Table III-1. Elements with $Z > 9$ were not fit with this function (III-5) because D3' saturates just beyond $Z = 9$, and the distribution widths are determined only by fluctuations

Figure III-6

Charge histogram indicating assignment of charge to events shown in Figure III-5, i.e., events with $P_c < 1.8$ GV. Method of assigning charge is discussed in text. Fitted curve is Equation III-5.

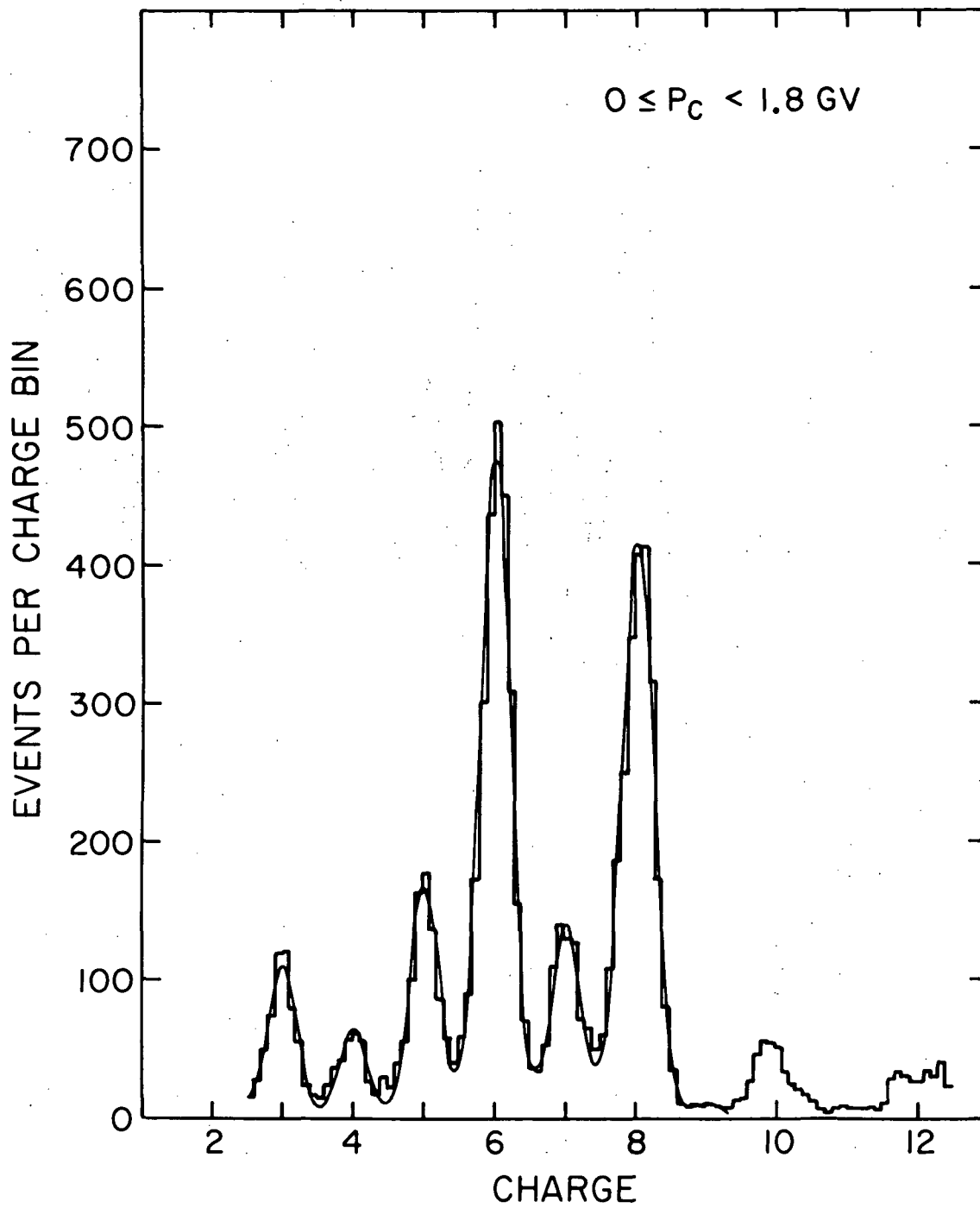
0 ≤ Pc < 1.8 GV
EVENTS PER CHARGE BIN
700
600
500
400
300
200
100
0
2
4
6
8
10
12
CHARGE

Figure III-6

Figure III-7

Charge histograms for events with $P_c \geq 1.8$ GV.

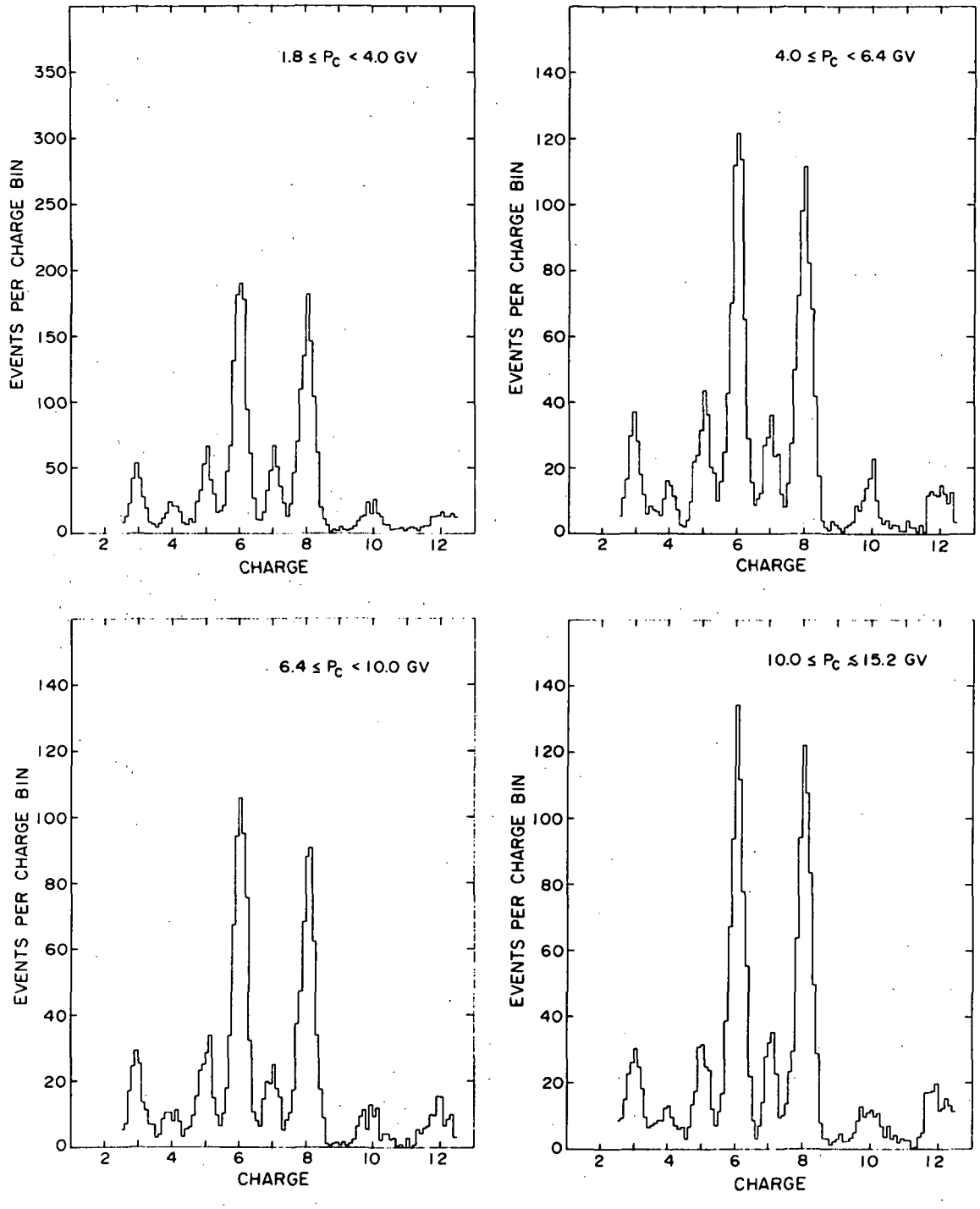
1.8 ≤ Pc < 4.0 GV
4.0 ≤ Pc < 6.4 GV
6.4 ≤ Pc < 10.0 GV
10.0 ≤ Pc ≲ 15.2 GV
EVENTS PER CHARGE BIN
CHARGE

Figure III-7

Table III-1. Results of Gaussian Fits (Equation III-5).

P_c, GV	0-1.8	1.8-4.0	4.0-6.4	6.4-10.0	10.0-15.2
A_3	106.4	42.2	28.6	24.2	27.2
A_4	63.1	25.7	14.6	12.1	13.7
A_5	164.1	55.3	40.2	31.0	31.6
A_6	475.4	189.3	114.4	100.5	118.2
A_7	137.4	53.9	33.2	23.0	29.6
A_8	413.6	163.9	105.6	87.5	118.1
A_9	10.4	3.2	1.8	1.2	3.4
a	1.0000	0.9997	0.9997	1.0023	1.0019
b	-0.0266	-0.0319	-0.0340	-0.0683	-0.0180
c	-0.0003	-0.0006	-0.0006	-0.0015	-0.0010
d	0.1987	0.2020	0.2032	0.2182	0.2252
10^3g	0.378	0.301	0.200	0.956	0.550
10^3h	0.502	0.368	0.366	0.165	-0.025
r	13.15	11.53	8.23	2.03	4.62
s	3.20	3.10	3.10	3.50	3.50
χ^2_ν	1.882	1.022	0.829	0.794	0.716

(χ^2_ν is the "reduced chi-squared" for the fit, given by χ^2/ν, where ν=55 is the number of degrees of freedom.)

in AVG'. Likewise, the fits were not extended below Z = 3 because of the gain changes of the detectors (See Figures II-3 and II-4), and the departure from Gaussian fluctuations for lower charges.

C. Abundance Ratios

For elements $3 \leq Z \leq 10$, relative abundances can be determined with good accuracy from charge histograms such as those shown in Figures III-6 and III-7. Such histograms were formed for several ranges of cutoff rigidity, and the function defined by Equations (III-5), (III-6), and (III-7) was fit to each using an iterative least-squares technique. The parameters c, d, and h of Equation (III-7) were also determined from a fit to <u>all</u> the data, and the individual data sets were fit again using the latter values of c, d, and h. The results of both procedures were consistent to within a few events for each charge, indicating that variations in the fitted σ values from one data set to the next are not significant, and have no effect on the relative abundances.

The number of events of each charge may be determined by integrating the appropriate Gaussian:

$$n_j = \int_{-\infty}^{\infty} A_j \exp[(z - z_j)^2/2\sigma_j^2]\, dz = \sqrt{2\pi}\, A_j \sigma_j \qquad \text{(III-8)}$$

and rounding to the nearest integer. We assume that the statistical accuracy of this procedure is limited by the Poisson statistics of the number of events thus derived. These numbers and key ratios are shown in Table III-2.

Since it was found that this procedure underestimated the area under the charge histograms, the following method was used to obtain

Table III-2. Number of Events Assigned to Each Charge, from Gaussian Fits.

P_c, GV	0-1.8	1.8-4.0	4.0-6.4	6.4-10.0	10.0-15.2
Li	540	215	147	131	149
Be	325	132	76	65	75
B	862	288	211	167	170
C	2560	1003	610	541	630
N	762	291	181	124	156
O	2367	905	587	475	616
F	62	18	10	7	18
Li/O	0.228±.011	0.238±.018	0.250±.023	0.275±.027	0.242±.022
Be/O	0.137±.008	0.146±.014	0.129±.016	0.137±.018	0.121±.015
B/O	0.364±.014	0.319±.022	0.359±.029	0.351±.032	0.276±.024
C/O	1.082±.031	1.109±.051	1.039±.060	1.140±.072	1.022±.058
N/O	0.322±.013	0.322±.022	0.308±.026	0.262±.026	0.253±.023
F/O	0.026±.003	0.020±.005	0.017±.006	0.014±.005	0.029±.007
Be/B	0.377±.025	0.458±.048	0.360±.048	0.390±.057	0.438±.061
L/M*	0.304±.008	0.289±.013	0.315±.017	0.318±.019	0.281±.016

* L/M = (Li+Be+B)/(C+N+O)

final charge assignments. The Gaussian functions derived for all charges, and the linear function for helium, were evaluated at each charge bin. The events in that bin were then assigned to the various charges in proportion to the relative values of the distribution functions. Thus, essentially all of the events near the center of distribution were assigned to that charge, while those falling between two distributions were split proportionately between them. This method assigns all the events in the histograms, and corrects for the possibility that Equations III-5, III-6, and III-7 may not be the best representation for the data. The results from this procedure are shown in Table III-3.

This table also shows helium abundances, which were obtained in a different way. For D1' and D2' pulse heights below the gain-change point (Figure II-3), we used the smaller of the two pulse heights as the measurement of the energy loss. This provides a considerable improvement in resolution by suppressing the long tail of the Symon distribution discussed earlier. For helium, it also has the advantage of removing most of the edge-effect events from the distribution. In addition, we require $|D1'-D2'| \leq 50$ channels, to discriminate against background caused by nuclear interactions and extreme Symon fluctuations. About 2% of the events are rejected by this method. The helium is quite clearly resolved from the singly charged distribution in the resulting MIN' *versus* D3' matrix (similar to Figure II-5), except at the lowest velocities, where the helium distribution overlaps the very large Symon tail from the singly charged distribution. For this reason, the helium

Table III-3. Number of Events Assigned to Each Charge, from Final Algorithm.

P_c, GV	0-1.8	1.8-4.0	4.0-6.4	6.4-10.0	10.0-15.2
He	107520	37220	24540	18710	23550
Li	547	222	157	136	151
Be	348	137	81	70	82
B	879	298	217	172	173
C	2577	1013	620	552	636
N	775	300	184	132	167
O	2391	917	593	483	623
F	54	18	12	6	16
He/O	45.0 ±1.0	40.6 ±1.4	41.4 ±1.7	38.7 ±1.8	37.8 ±1.5
Li/O	0.228±0.011	0.242±0.018	0.265±0.024	0.281±0.028	0.243±0.022
Be/O	0.146±0.008	0.149±0.014	0.137±0.016	0.146±0.019	0.132±0.015
B/O	0.367±0.014	0.325±0.022	0.367±0.029	0.357±0.032	0.278±0.024
C/O	1.077±0.031	1.106±0.050	1.047±0.060	1.143±0.071	1.022±0.058
N/O	0.324±0.013	0.328±0.022	0.311±0.026	0.273±0.027	0.268±0.023
F/O	0.022±0.003	0.019±0.005	0.020±0.006	0.013±0.005	0.027±0.007
Be/B	0.396±0.025	0.459±0.047	0.374±0.049	0.408±0.058	0.474±0.064
L/M	0.309±0.008	0.295±0.013	0.326±0.018	0.324±0.019	0.285±0.016

abundance for $P_c < 1.8$ GV is uncertain by about 5 - 8% in addition to the statistical uncertainty. For $P_c \gtrsim 1.8$ GV this presents no problem, since the geomagnetic cutoff prevents low-velocity helium from entering the telescope. Determination of the helium abundance is therefore simply a matter of counting the events within a specified region of MIN' *versus* D3' space.

IV. Results and Interpretation

A. Integral Rigidity Spectra

In order to obtain rigidity spectra, we make use of counting-rate information supplied by the Čerenkov rate scaler. This scaler counts all events which satisfy the D2'D3'$\overline{D4}$' coincidence requirement, and is read out once every 432 msec. During this period, a maximum of three events can be analyzed by the pulse-height analysis system. However, due to the special design of the rate accumulator (*Althouse et al.*, 1967), the maximum counting rate ($\sim 10^4$ sec^{-1}) is limited only by the recovery time of the discriminators.

Because OGO-6 is in a polar orbit, it spends a certain fraction of its time in regions of high trapped-particle flux. Data taken under those conditions are deleted as discussed in Appendix B. For the remaining data, the following quantities are accumulated in bins of cutoff rigidity (P_c) 0.08 GV wide:

R = number of Čerenkov scaler readouts,

C = number of coincidences counted by scaler,

N = number of Čerenkov events analyzed.

The total flux of particles in any bin is given by

$$J = C/.432RA\Omega \ (\mathrm{cm}^2\cdot\mathrm{sec}\cdot\mathrm{ster})^{-1} \qquad \text{(IV-1)}$$

where $A\Omega \simeq 3.4$ cm^2·ster is the geometrical factor corresponding to the D2'D3'$\overline{D4}$' geometry, including detector edge regions as discussed earlier.

The analyzed events can be assigned charges, as discussed in Chapter III, or may be rejected because of D1"-D2' inconsistency. If we designate these as n_Z and n_R, respectively, then

$$N = n_R + \sum_Z n_Z \ . \qquad \text{(IV-2)}$$

Since we have determined that there is no significant charge dependence in the criteria for event selection, n_R should be composed of events of all charges, in proportion to their relative flux. Also, it is reasonable to assume that events are analyzed in proportion to their respective fluxes, so

$$n_z/\sum_z n_z = J_z/J \quad , \qquad \text{(IV-3)}$$

or

$$J_z/J = n_z/(N - n_R) \quad . \qquad \text{(IV-4)}$$

However, since most of the rejected events are due to geometrical edge effects (as discussed earlier), it is equivalent to correct the geometrical factor to compensate for the rejection of these events. We define

$$G = A\Omega(\sum_Z n_Z/N) = A\Omega(1 - n_R/N) \ . \qquad \text{(IV-5)}$$

The flux of a given charge component is then given by

$$J_Z = (C/.432\ RG)\ (n_Z/N) = Jn_Z/(N - n_R)\ . \qquad \text{(IV-6)}$$

There is some uncertainty in this procedure, because the event selection criteria described earlier apply only for $3 \leq Z \leq 12$. Different criteria are applied for $Z < 3$, resulting in a possible systematic uncertainty of $\sim$2 - 3% in the absolute fluxes, in addition to the $\sim$6% uncertainty in $A\Omega$. This problem does not affect abundance ratios for $3 \leq Z \leq 10$, however, since

$$J_Z/J_{Z'} = n_Z/n_{Z'}\ . \qquad \text{(IV-7)}$$

An independent estimate of $G/A\Omega$ can be obtained by calculating geometrical factors directly. We assume G is defined by the gold evaporation on the surface-barrier detectors. This was determined to give a diameter of 2.34 cm ± 3%, yielding $G = 2.75\ cm^2 \cdot ster \pm 6\%$. We estimate from the construction of the detectors that the edge region may be 1 - 1.5 mm wide. This would give an effective diameter of 2.54 - 2.64 cm, or $A\Omega \simeq 3.2 - 3.5\ cm^2 \cdot ster$. This results in a ratio $G/A\Omega \simeq 0.78 - 0.86$, which is compatible with the value 0.81 obtained from Equation IV-5.

Integral rigidity spectra for $2 \leq Z \leq 10$ are shown in Figures IV-1 to IV-3. Error limits in these figures represent only the statistical uncertainties associated with n_Z for each rigidity bin. The curves represent the helium spectrum of Figure IV-1 multiplied by a suitable

Figure IV-1

Integral rigidity spectra of helium, oxygen, lithium, and fluorine. The statistical errors in the helium fluxes are comparable to the size of the symbols. Fluxes are averaged over cutoff rigidity bins having edges at multiples of 0.64 GV (0.16 GV for He). Note that all the points are statistically independent. The curves have the shape of the helium spectrum, with normalization determined from fits as discussed in the text.

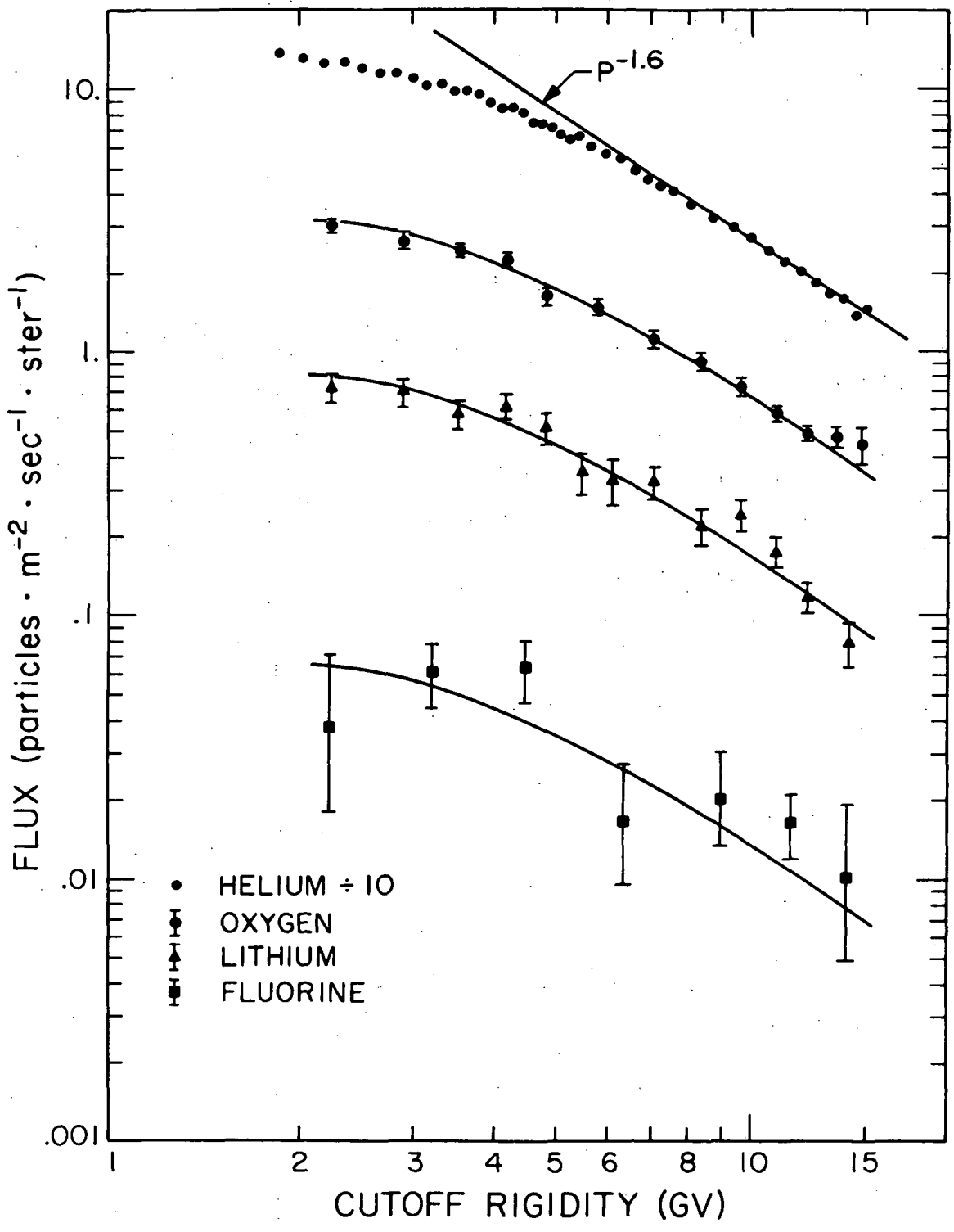
$P^{-1.6}$
10.
1.
.1
.01
.001
FLUX (particles · m^{-2} · sec^{-1} · ster^{-1})
HELIUM ÷ 10
OXYGEN
LITHIUM
FLUORINE
1
2
3
4
5
6
8
10
15
CUTOFF RIGIDITY (GV)

Figure IV-1

Figure IV-2

Integral rigidity spectra of beryllium, boron, and carbon. The fitted curves are derived from the helium spectrum of Figure IV-1.

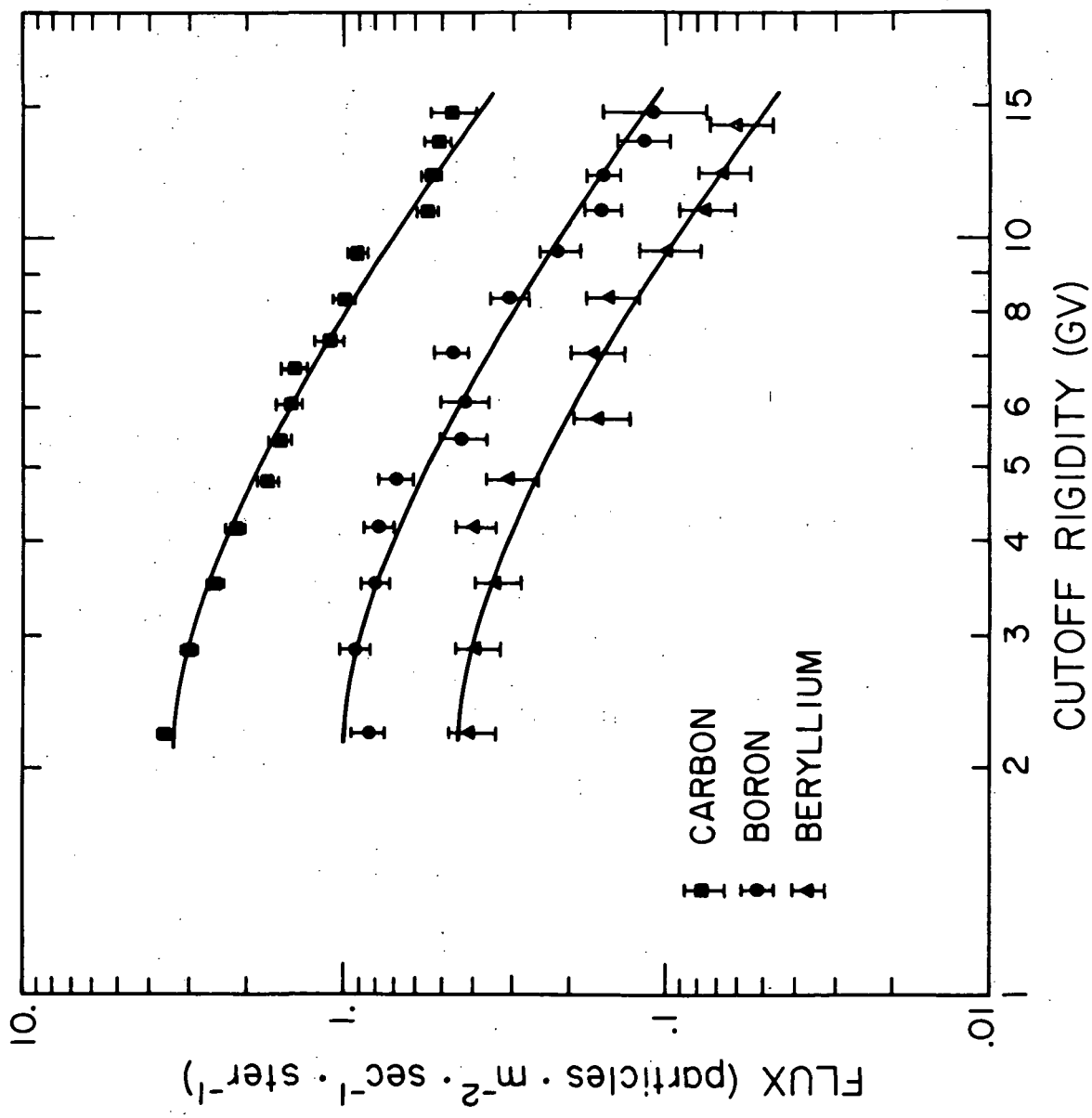
FLUX (particles · m^{-2} · sec^{-1} · ster^{-1})
10.
1.
.1
.01
CUTOFF RIGIDITY (GV)
2
3
4
5
6
8
10
15
CARBON
BORON
BERYLLIUM

Figure IV-2

Figure IV-3

Integral rigidity spectra of nitrogen and neon. The fitted curves are derived from the helium spectrum of Figure IV-1.

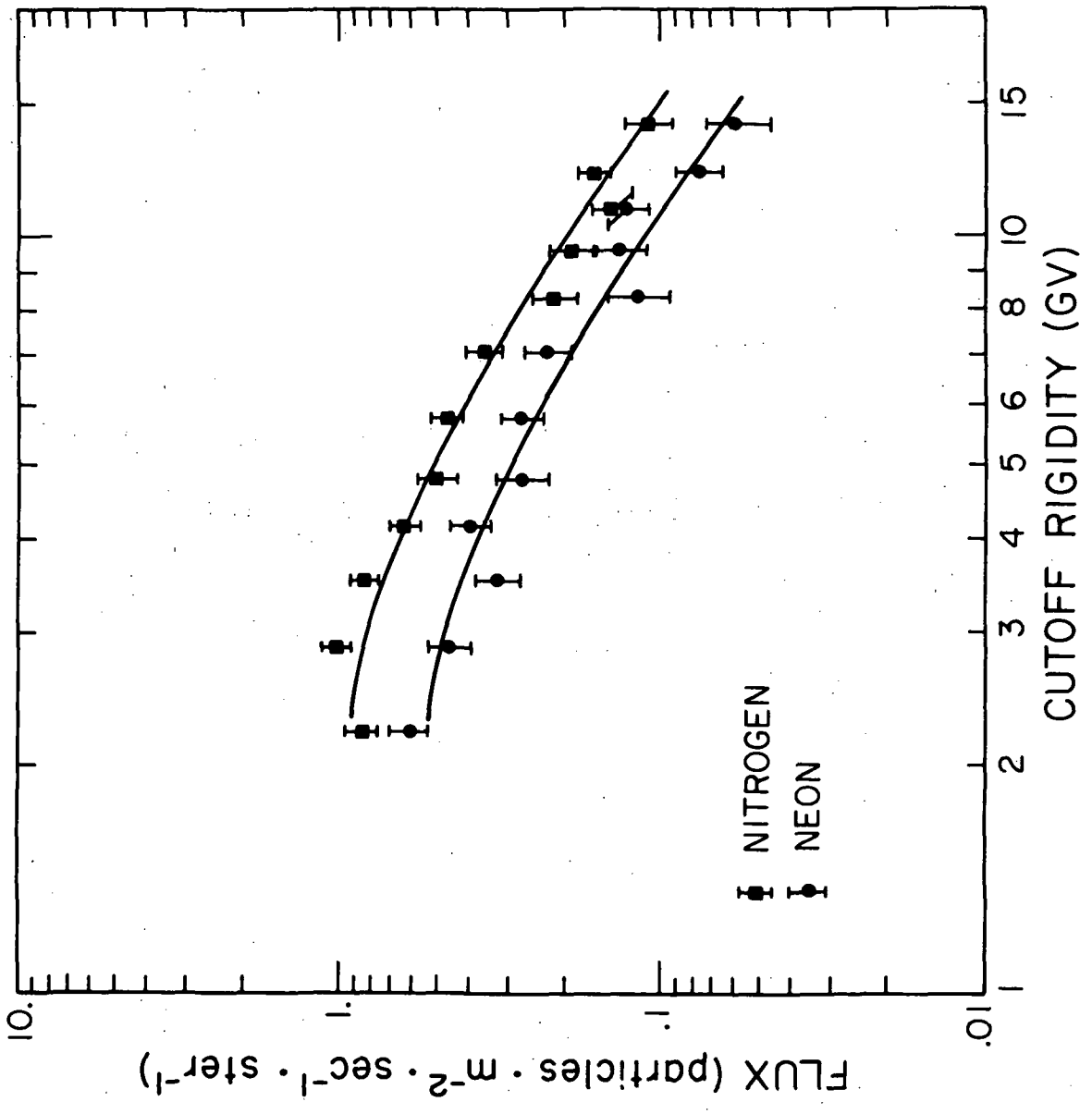
FLUX (particles · m^{-2} · sec^{-1} · ster^{-1})
10.
1.
.1
.01
1
2
3
4
5
6
8
10
15
CUTOFF RIGIDITY (GV)
NITROGEN
NEON

Figure IV-3

constant in each case. The constants were determined from least-squares fits of the spectral points shown in the figures to the helium spectral points corresponding to the same range of cutoff rigidities. The results of these fits are shown in Table IV-1. The last column of this table contains the probabilities that larger values of x^2 would be obtained if the experiment were repeated. It is clear from this table and from Figures IV-1 to IV-3 that all the spectra have the same shape, within the limits of our statistics.

In Table IV-2 we compare the abundances relative to helium as derived above with those obtained by summing the individual abundances from Table III-3. We use only the data for $P_c \geq 1.8$ GV for the latter calculation, because the data for $P_c < 1.8$ GV were not included in the spectral fits. The excellent agreement of the results obtained by these two methods is further support for the claim that there are no statistically significant differences in the shapes of the spectra.

Table IV-1. Results of Fits to Helium Spectrum.

	Ratio	χ^2	ν	χ^2_ν	$P(>\chi^2)$
Li/He	.0064	11.8	12	0.98	0.47
Be/He	.0036	7.5	11	0.68	0.76
B/He	.0081	14.2	13	1.09	0.36
C/He	.0270	20.6	14	1.47	0.12
N/He	.0074	11.5	11	1.05	0.40
O/He	.0251	9.6	12	0.80	0.65
F/He	.0005	8.2	6	1.37	0.23
Ne/He	.0042	10.8	11	0.98	0.46

The number of degrees of freedom for each fit is ν; χ^2_ν is χ^2/ν.

Table IV-2. Abundances Normalized to Helium.

	From Table III-3*	From Table IV-1
Li/He	.00640±.00025	.0064
Be/He	.00356±.00019	.0036
B/He	.00827±.00028	.0081
C/He	.0271 ±.0005	.0270
N/He	.00753±.00027	.0074
O/He	.0252 ±.0005	.0251
F/He	.00050±.00007	.0005

*Sums for $1.8 \leq P_c < 15.2$ GV

B. Abundance Ratios and Interstellar Propagation

The purpose of making these measurements of the nuclear component of the cosmic radiation is to gain information concerning the sources, confinement, and propagation of the radiation in the galaxy. At the present time, the simplest model which has had reasonable success in fitting experimental data is the steady-state model of Cowsik *et al.* (1967), in which the assumptions of steady-state source injection, rapid diffusion, and slow leakage from the galaxy produce an exponential distribution of cosmic-ray path lengths. Inclusion of the effects of ionization energy loss, nuclear interactions, and the decay of ^{10}Be to ^{10}B complete the picture.

The formulation we use is that of Meneguzzi *et al.* (1971), which is somewhat similar to that of Gloeckler and Jokipii (1969). Following Meneguzzi *et al.*, we write the continuity equation:

$$\frac{\partial N_i}{\partial t} = 0 = -\frac{N_i(E)}{\tau_e} - \frac{N_i(E)}{\gamma\tau_i} + \sum_k \frac{N_k(E)}{\gamma\tau_{ki}} + Q_i(E)$$

$$+ \frac{\partial}{\partial E}[b_i(E)N_i(E)]$$

$$- [\sigma_{\alpha i}(E)n_{He} + \sigma_{pi}(E)n_H]v_i N_i(E)$$

$$+ \sum_{j>i}[\sigma_{\alpha ji}(E)n_{He} + \sigma_{pji}(E)n_H]v_j N_j(E) \qquad \text{(IV-8)}$$

where we have made the usual assumption that secondaries produced in nuclear interactions have the same energy/nucleon as the primary. The first term replaces a diffusion term in the "leaky-box" approximation: τ_e is the mean lifetime against escape from the galaxy. The second term represents loss of i-type particles by radioactive decay with mean life τ_i; the third term, which we have added, represents production of i-type nuclei through $k \rightarrow i$ decay with mean life τ_{ki}. Of course, these terms are used only for $^{10}Be \rightarrow {}^{10}B$ decay in the range of charges we are considering. $Q_i(E)$ is the source injection spectrum. The rate of energy loss due to ionization is $b_i(E) = dE/dt = v_i \rho dE/dx$, where ρ is the density of the gas: $n_H M_H + n_{He} M_{He}$. The cross sections for destruction are $\sigma_{\alpha i}$ for destruction on helium and σ_{pi} for destruction on hydrogen. Partial cross sections for production are given by $\sigma_{\alpha ji}$ (for $j + \alpha \rightarrow i$) and σ_{pji} (for $j + p \rightarrow i$). These include production of unstable nuclei which decay rapidly ($\tau << 10^5$y) to i-type nuclei. Finally, v_i is the particle velocity; n_{He} and n_H are the number densities of helium and hydrogen in the interstellar gas. These equations can be solved (*Gloeckler and Jokipii*, 1969; *Meneguzzi et al.*, 1971), giving a triangular system of equations in the N_i. The equation for iron is solved first (iron is assumed to be entirely primary), then the equation for each lighter nuclide is solved in turn.

We have made the modification of including as a source of ^{10}B all the ^{10}Be that decays. This is a relatively small correction, amounting to about 10% of the ^{10}B flux, or about 3% of the total boron; but it is neglected by Meneguzzi *et al.* In addition, we have used the latest value for the ^{10}Be half-life: 1.5×10^6 y (*Yiou and Raisbeck*, 1972).

The model includes nuclear interactions with interstellar helium as well as hydrogen. We assume that the interstellar gas is composed of one hydrogen atom and 0.1 helium atom per cubic centimeter. The assumed source composition is shown in Table IV-3. This is basically the same as that used by Meneguzzi *et al.*, but we have adjusted the ^{4}He, ^{14}N, and ^{16}O abundances slightly to fit our data. The source spectra are assumed to be power laws in total energy, with exponent -2.6. The escape mean free path, Λ_e, is a free parameter.

The result of the calculation is a differential energy spectrum for each isotope from ^{1}H to ^{16}O, plus ^{20}Ne, ^{24}Mg, ^{28}Si, and ^{56}Fe. To compare these results with our data, we convert each differential energy spectrum to an integral rigidity spectrum, sum the resulting fluxes over all the isotopes of each element, and divide by the oxygen flux. The results are shown as the dashed lines in Figures IV-4 and IV-5; the data points are taken from Table III-3. Abundance ratios shown are calculated for Λ_e = 6, 8, and 10 g/cm^2. Neglecting interstellar helium would have resulted in higher predicted ratios, or lower values of Λ_e deduced from the data. The difference in Λ_e is approximately 1 g/cm^2. The curves shown in the figures would thus correspond to $\Lambda_e \approx$ 5, 7, and 9 g/cm^2 if the helium were not included in the calculations. Our calculated L/M for Λ_e = 6 g/cm^2 would agree very closely with that calculated by Mason (1972) if we neglected the interstellar helium.

We cannot compare the data directly to these curves, because the modulation of galactic cosmic rays by the solar wind may be expected to alter the composition. This problem is particularly severe for our data which were obtained during solar maximum. The usual procedure for

Table IV-3. Assumed Cosmic Ray Source Abundances.

Isotope	Abundance (this work)	SST	WDK
^{4}He	32±1	27±5	-
^{12}C	1†	1†	1†
^{14}N	0.07*	0.12±.03	0.110±.016
^{16}O	1.2±0.1	1.02±.06	1.06
^{20}Ne	0.25**	0.20±.03	0.17
^{24}Mg	0.29**	0.27±.04	0.23
^{28}Si	0.26**	0.23±.04	0.17
^{56}Fe	0.25**	0.23±.05	0.19

†Normalization

*This value was used to calculate the curves in Figure IV-5. The data appear to imply a value of 0.10±.01 for N/C at the source.

**Abundances of elements heavier than oxygen are taken from Meneguzzi *et al.* (1971), who adjusted them to compensate for the neglect of secondary 14<Z<26.

SST - Shapiro *et al.* (1971)

WDK - Webber *et al.* (1972)

Figure IV-4

Ratios Li/O, Be/O, and B/O with predicted interstellar values (dashed lines), and values at 1 A.U. (solid lines). Numbers at right are values of escape mean free path, Λ_e, in g/cm^2. Neglecting interstellar helium yields similar curves with Λ_e decreased by ~1 g/cm^2 for each curve.

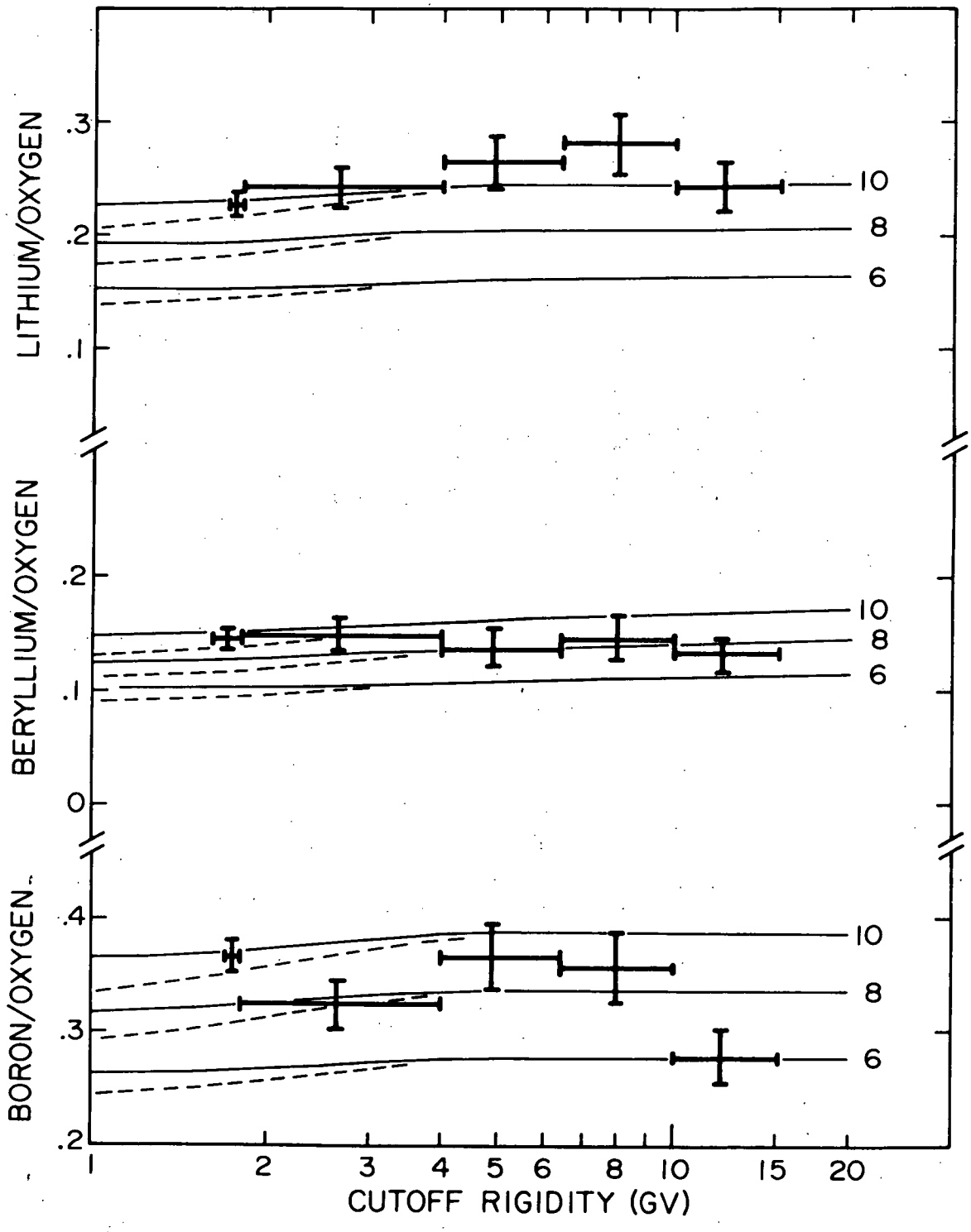
LITHIUM/OXYGEN
.3
.2
.1
10
8
6
BERYLLIUM/OXYGEN
.2
.1
0
10
8
6
BORON/OXYGEN
.4
.3
.2
10
8
6
1
2
3
4
5
6
8
10
15
20
CUTOFF RIGIDITY (GV)

Figure IV-4

Figure IV-5

Ratios He/O, C/O, and N/O. Source abundances were adjusted to fit data.

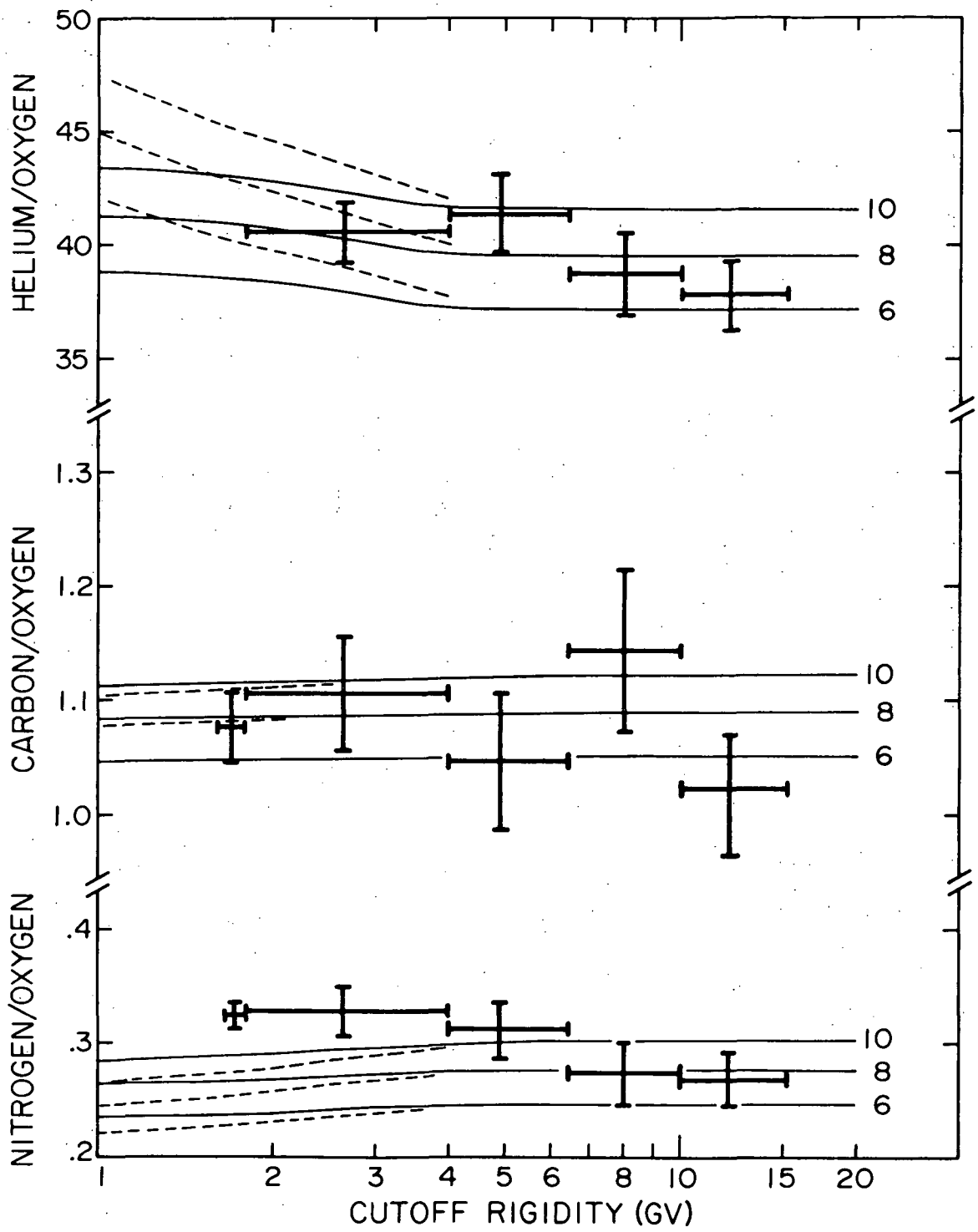
HELIUM/OXYGEN
50
45
40
35
10
8
6
CARBON/OXYGEN
1.3
1.2
1.1
1.0
10
8
6
NITROGEN/OXYGEN
.4
.3
.2
10
8
6
1
2
3
4
5
6
8
10
15
20
CUTOFF RIGIDITY (GV)

Figure IV-5

attacking this problem is to make some assumptions about the functional form of the modulation, estimate its effect on the abundance ratios, and extrapolate the observations to interstellar space.

We take the opposite approach here: the fluxes calculated from the interstellar propagation model are used as boundary conditions for numerical solutions of the transport equation governing the motion of cosmic rays in the interplanetary medium:

$$\partial U/\partial t = - \vec{\nabla}\cdot(\vec{V}_W U) + \tfrac{1}{3}[(\vec{\nabla}\cdot\vec{V}_W)\partial(\alpha TU)/\partial T] + \vec{\nabla}\cdot(\bar{\bar{\kappa}}\cdot\vec{\nabla}U) \qquad \text{(IV-9)}$$

where U is the number of particles per unit volume per unit interval of kinetic energy, $\vec{V}_W$ is the solar wind velocity, T is the kinetic energy, $\bar{\bar{\kappa}}$ is the diffusion tensor, and $\alpha = (T + 2M)/(T + M)$, where M is the particle's rest energy. This description of solar modulation has recently been reviewed by Jokipii (1971).

Equation IV-9 may be simplified by making the following assumptions:

1) spherical symmetry,
2) constant, radial solar wind velocity,
3) no time dependence,
4) no modulation beyond a certain radial distance, D.

Using these assumptions, we get (*Garrard*, 1973):

$$r^{-2}V_W\partial(r^2U)/\partial r - (2V_W/3r)\partial(\alpha TU)/\partial T - r^{-2}\partial(r^2\kappa\partial U/\partial r)/\partial r = 0 \qquad \text{(IV-10)}$$

to be solved with the boundary condition U(T,r=D) = U(T,interstellar). Here κ is the radial part of the diffusion tensor.

The solution we use is that of Garrard (1973), with the following parameters: $D = 6.1$ AU, $V_W = 400$ km/sec, and $\kappa = k_0 \beta f(R)$, where $f(R) = R$ for $R \geq R_0$, $f(R) = \sqrt{RR_0}$ for $R < R_0$, $R_0 = 1.5$ GV, and $k_0 = 1.1 \times 10^{21}$ $cm^2 \cdot sec^{-1} \cdot GV^{-1}$. These parameters were determined (*Cummings*, 1973; *Garrard*, 1973) for 1969, when most of our data were taken. The transport equation is solved separately for each isotope; the resulting fluxes at 1 A.U. are converted to integral rigidity spectra; these are summed over all isotopes of each element and divided by the oxygen spectrum. The resulting ratios are shown as the solid lines in Figures IV-4 and IV-5.

A number of conclusions can be drawn from Figure IV-4, which shows the abundances, relative to oxygen, of the "light" elements, which are assumed to be absent from the sources. First, it appears that the beryllium/oxygen and boron/oxygen ratios both correspond to $\Lambda_e \simeq 10$ g/cm^2 at $\sim$2 GV, decreasing to 6 or 7 g/cm^2 at 10-15 GV. (The boron point at 1.8-4 GV apparently is low due to a statistical fluctuation, as may be seen by examining the boron spectrum in Figure IV-2.) A dependence of escape mean free path on rigidity was suggested by Cowsik *et al.* (1967), but has since been neglected by most authors (*e.g.*, *Shapiro et al.*, 1970; *Webber et al.*, 1972; *Mason*, 1972), usually in favor of a model employing an exponential distribution with the short path lengths suppressed. Von Rosenvinge *et al.* (1969) conclude that the lack of variation of L/M (the commonly used ratio [Li + Be + B]/[C + N + O]) with energy is evidence for a path length distribution which is either a delta-function or a Gaussian with a very small width. More recently it has been pointed out (*Mason*, 1972) that the constancy of this ratio at low energies ($\lesssim$300 MeV/nucleon) is evidence for adiabatic deceleration of the cosmic

rays in the expanding solar wind. At intermediate energies, such as those we observe, small solar modulation effects may combine with a variation in Λ_e with rigidity (or energy) to produce a nearly energy-independent L/M. At higher energies ($\gtrsim$4 GeV/nucleon) a decrease of secondaries/primaries with increasing energy (*Juliusson et al.*, 1972; *Webber et al.*, 1973; *Smith et al.*, 1973) points strongly towards an energy-dependent leakage mean free path.

The second observation we make from Figure IV-4 is that there appears to be too much lithium, if we assume that the Λ_e implied by beryllium and boron is correct. There are four possible explanations for this: 1) currently assumed cross sections for producing lithium from heavier cosmic rays are too small, 2) the assumed total inelastic cross sections for destroying ^{6}Li and ^{7}Li are too large, 3) there is some thermonuclear ^{7}Li present in the cosmic ray sources, and 4) our measurement is wrong.

The last possibility would seem to be the simplest explanation, since it is rather difficult to separate lithium completely from spillover from the very large helium peak. We have examined the helium distributions in all our detectors, and carefully corrected the lithium for contamination from this source. The probability that 30% of our remaining lithium is still misidentified helium is rather small, but probably non-zero.

Possibilities (1) and (2) above certainly cannot be ruled out. Measurements of fragmentation of L nuclei in nuclear emulsions (*Cleghorn*, 1967) indicate that the isotopes of lithium and beryllium may be exceptional cases which do not agree with predictions of cross

sections based on geometrical or semi-empirical (*e.g.*, *Silberberg and Tsao*, 1971) formulas. Extensive cross section measurements will be required to resolve this point.

The third possibility is the most interesting from an astrophysical point of view. The existence of a source of interstellar ^{7}Li was proposed by Meneguzzi *et al.* (1971) to explain the large ^{7}Li/^{6}Li ratio observed on the earth and moon, and in meteorites and some stars. The existence of a substantial amount of ^{7}Li in cosmic-ray sources would seem unlikely, however, because the deduced source abundances of the heavier elements indicate that the sources are highly evolved objects, such as supernovae, which would probably not contain sufficient lithium to account for this observation. Similar discrepancies in the measured lithium abundances have appeared previously (*Von Rosenvinge et al.*, 1969; *Mason*, 1972), indicating either the difficulty of making an unambiguous determination of the lithium abundance, or the necessity of revising the model.

In Figure IV-5 we show ratios of elements which presumably are present at the cosmic ray sources. As mentioned previously, the source abundances have been adjusted to fit the data, although it appears from the figure that we may have underestimated the nitrogen abundance in the source by about .03. The important feature to be noted here is that the helium and nitrogen (and possibly the carbon) also show the tendency toward shorter path lengths at higher rigidities. This is independent of the assumed source abundances, and requires only that all the source spectra have the same shape.

We conclude (1) that an escape mean free path varying from $\sim$10 g/cm^2 at $\gtrsim$2 GV to $\sim$6 g/cm^2 at $\gtrsim$10 GV enables the simple "leaky box" model to fit the data quite well, and that no modifications to the exponential path-length distribution are necessary; and (2) that individual element ratios, such as Be/O, are superior to combined ratios, such as L/M, for testing propagation models. Of course, individual isotope ratios will be even more enlightening when they become available.

For comparison we show some published results of other authors, with our calculations and data for some of the combined ratios. Figure IV-6 shows the L/M ratio obtained by Mason (1972) on the IMP-5 spacecraft. The dotted curve is his calculation based on an exponential path-length distribution with a mean of 6 g/cm^2, which would correspond to $\Lambda_e \simeq$ 7 g/cm^2 if helium is included. Some balloon results are shown in Figure IV-7. These have been extrapolated to the top of the atmosphere by Webber *et al.* (1973). These results are strong evidence for a continuing decrease in the Λ_e with increasing energy.

Our underestimation of the amount of nitrogen in the cosmic ray sources, and the ambiguity in the comparison of calculated and measured lithium, are examples of the pitfalls inherent in the use of ratios of this type. The improvement in statistics obtained by combining all the L elements is more than offset by the increased difficulty of interpreting the results correctly.

Finally, we turn to the problem of estimating the confinement time, or "age" of the cosmic rays by examining the effect of ^{10}Be decay. This problem has never been completely resolved, because of the poor statistics involved in measuring beryllium, the uncertainties in the cross

Figure IV-6

L/M from this experiment (upper panel) and from Mason (1972, lower panel). Solid curves are predicted values at 1 A.U., for values of Λ_e specified at right. Dotted curve is Mason's calculation for $\Lambda_e = 6$ g/cm^2, with no interstellar helium.

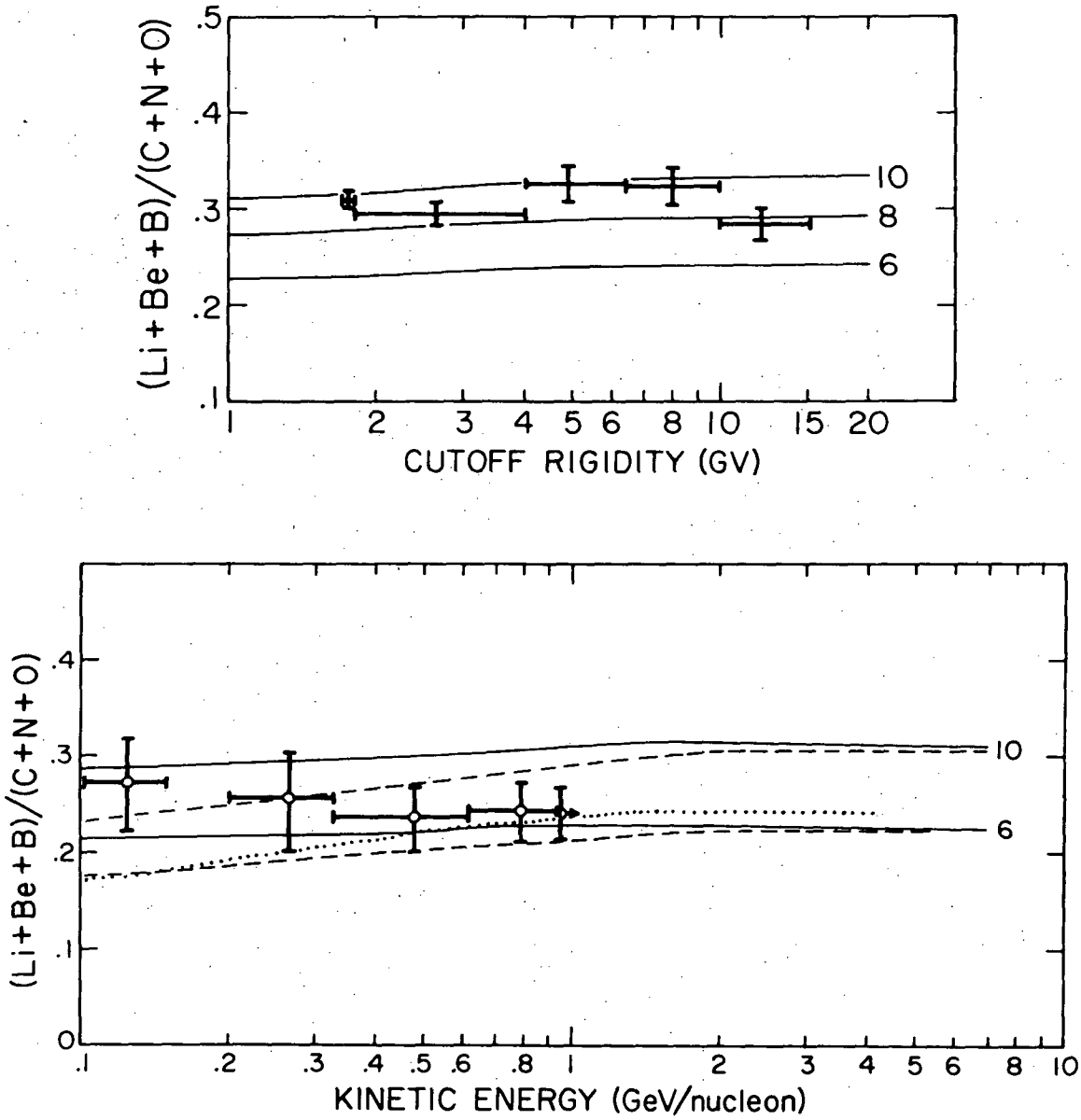
(Li+Be+B)/(C+N+O)
.5
.4
.3
.2
.1
10
8
6
1
2
3
4
5
6
8
10
15
20
CUTOFF RIGIDITY (GV)
(Li+Be+B)/(C+N+O)
.4
.3
.2
.1
0
10
6
.1
.2
.3
.4
.5
.6
.8
1
2
3
4
5
6
8
10
KINETIC ENERGY (GeV/nucleon)

Figure IV-6

Figure IV-7

L/(C + O) from this experiment (upper panel) and from balloon measurements as indicated. Balloon data were extrapolated to the top of the atmosphere by Webber *et al.*, who also converted the Berkeley data from rigidity to energy intervals.

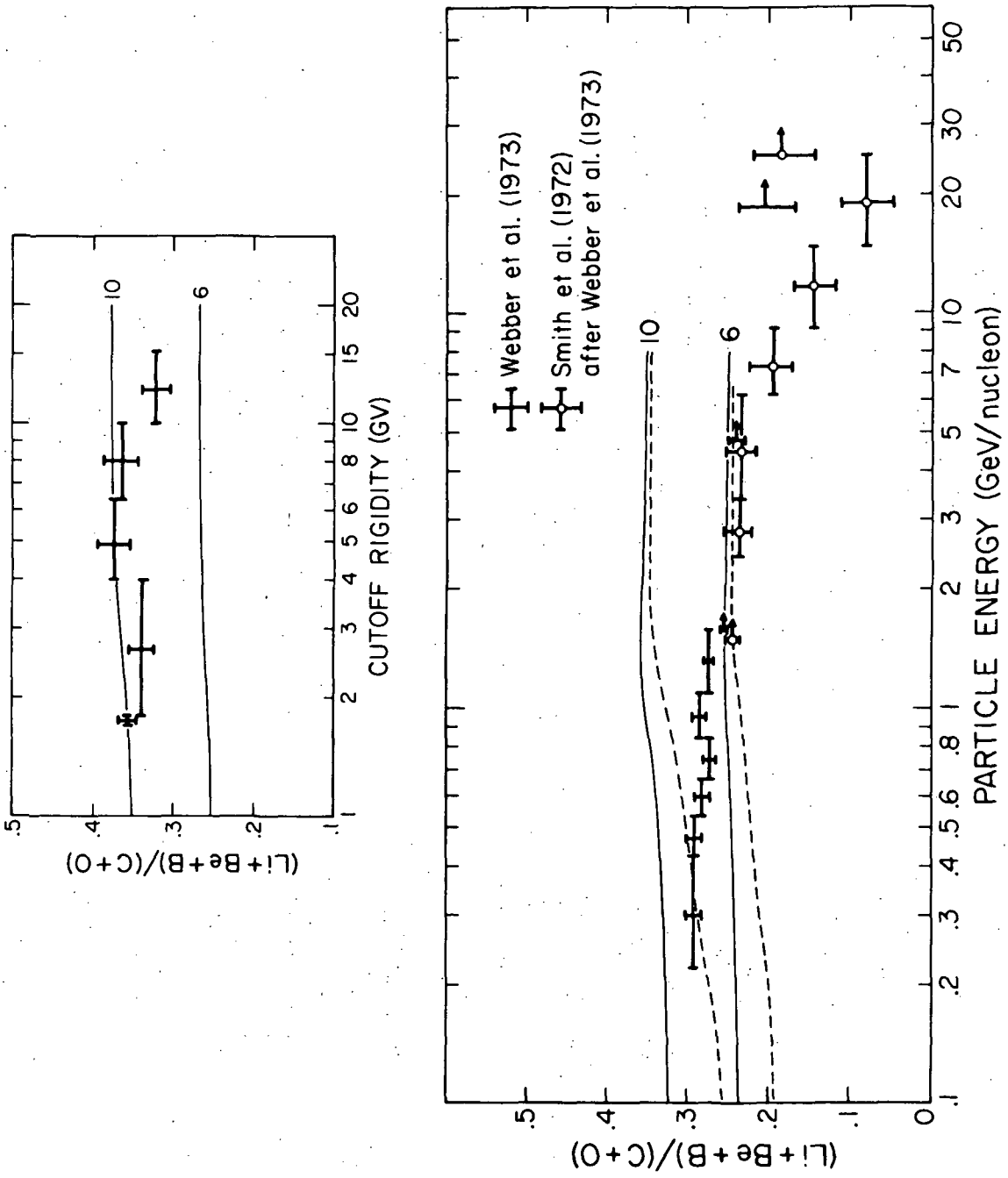
(Li + Be + B)/(C + O)
CUTOFF RIGIDITY (GV)
10
6
Webber et al. (1973)
Smith et al. (1972)
after Webber et al. (1973)
PARTICLE ENERGY (GeV/nucleon)

Figure IV-7

sections, and smallness of the expected effect. Some authors have claimed or implied substantial decay of ^{10}Be (*Lezniak et al.*, 1970; *Webber et al.*, 1972) while others have claimed survival (*Von Rosenvinge et al.*, 1969; *O'Dell et al.*, 1971).

Our results are shown in Figure IV-8, where we have used a value of 8 g/cm^2 for Λ_e, and varied the average density of the interstellar hydrogen from 0.1 to 10 cm^{-3}, keeping He/H = 0.1. The average confinement time, τ_e, can be related to Λ_e by

$$\tau_e = \Lambda_e/\beta c(n_H M_H + n_{He} M_{He}) \qquad \text{(IV-11)}$$

where n and M are the appropriate number densities and masses. For $n_H = 1$ cm^{-3}, $\tau_e \simeq 1.14 \times 10^{14}/\beta$ sec $\simeq 3.5 \times 10^6/\beta$ years. Our data appear to favor a value of n_H not too different from 1 cm^{-3}, so a lifetime of a few million years is implied. Our ratio for Be/B for all data with $P_c \geq 1.8$ GV is 0.43 ± 0.03. This is only 0.15 standard deviation from the value calculated by O'Dell *et al.* (1971) for ^{10}Be survival, but is 2.5 standard deviations from their value assuming decay of ^{10}Be. From the Be/B ratio for $P_c < 1.8$ GV, we obtain a mean confinement time of $10^{6.5\pm0.5}$ years. The points at higher rigidities, when averaged together, imply $\tau_e \lesssim 10^7$ years.

There may be some additional effect due to the variation of Λ_e with rigidity, but it will not be possible to investigate this until much better data are available (at least 10^4 Be events, preferably observed at solar minimum) and until all the appropriate cross sections are accurately measured or reliably estimated.

Figure IV-8

Ratio Be/B. Solid curves are predicted values at 1 A.U. Numbers at right are average density of interstellar hydrogen, in atoms/cm^3. Helium density is one-tenth of hydrogen density in each case. Curves are calculated using $\Lambda_e = 8$ g/cm^2.

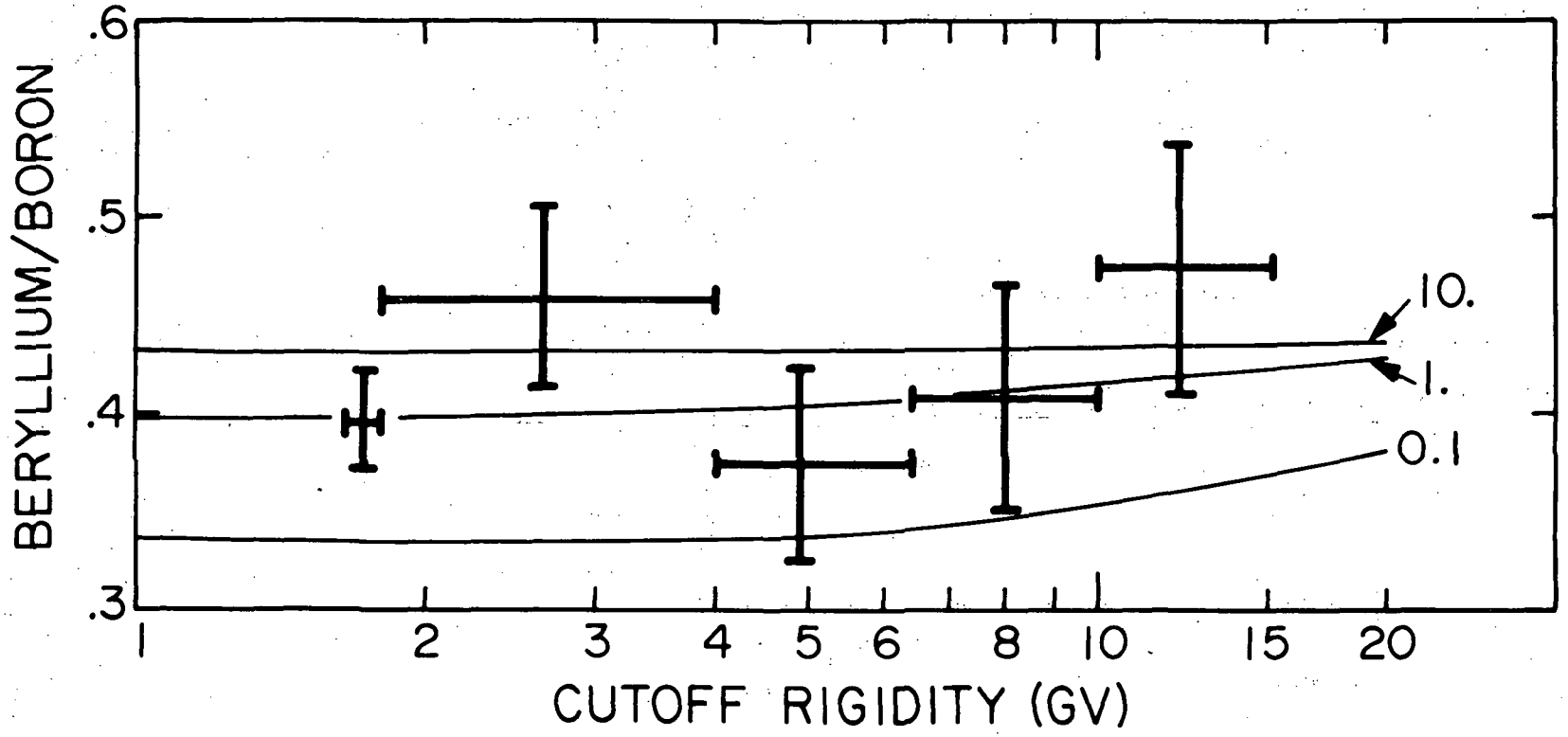
BERYLLIUM/BORON
.6
.5
.4
.3
1
2
3
4
5
6
8
10
15
20
CUTOFF RIGIDITY (GV)
10.
1.
0.1

Figure IV-8

V. Summary and Conclusions

We have made the first comprehensive satellite measurement of the abundances and spectra of cosmic ray nuclei using the geomagnetic field as a spectral analyzer. This was made possible by the low-altitude polar orbit of the OGO-6 spacecraft, and its attitude control system which kept the Caltech experiment aimed radially away from the earth. The advantages of this type of measurement over the more common method of using high-altitude balloons are (1) the ability to sample a wide range of cutoff rigidities, and (2) the elimination of the difficult problem of correcting for atmospheric secondaries. The instrument used the technique of making simultaneous measurements of energy loss and Čerenkov radiation.

By making a very careful and extensive study of the properties of the instrument, we were able to obtain data with very low background, good charge resolution ($\sigma \simeq 0.2$ charge unit), and negligible charge-dependent bias. This was done using a relatively simple instrument, containing a minimum of mass which might induce nuclear interactions.

We found that all the elements $2 \leq Z \leq 10$ have similar integral spectra over the range of cutoff rigidities from $\sim$2 to $\sim$15 GV, approaching a $P^{-1.6}$ power law at rigidities $\gtrsim$8 GV. Ratios of various elements are essentially independent of rigidity over the range observed. The values of the ratios and their dependence (or lack thereof) on rigidity, combined with calculations of interstellar propagation and solar modulation imply the following conclusions:

1) A simple "leaky box" model for galactic confinement of cosmic rays is adequate to explain the data.

2) The leakage, expressed as a mean free path, must vary with rigidity, having a value decreasing from $\sim$10 g/cm^2 at $\sim$2 GV to $\sim$6 or 7 g/cm^2 at $\sim$10 GV.

3) The effect of interstellar helium on the propagation of cosmic rays cannot be neglected.

4) The effect of solar modulation on elemental abundance ratios is important for rigidities less than 3 or 4 GV (kinetic energies $\lesssim$1 or 2 GeV/nucleon), and is probably dominant below 200 or 300 MeV/nucleon, at solar maximum.

5) Individual element ratios, such as beryllium/oxygen, are preferable to combined ratios, such as L/M, for testing propagation models.

6) Accurate measurements of production and destruction cross sections for the isotopes of lithium, beryllium, and boron will be needed before finer details of the propagation can be studied.

7) The ratio of beryllium/boron implies an average density of neutral hydrogen of about 1 /cm^3 and a mean confinement time of $10^{6.5\pm0.5}$ years. Survival of most of the ^{10}Be is favored. This implies confinement of the cosmic rays mainly within the galactic disc.

APPENDIX A. Data Processing and Assignment of Cutoff Rigidities

It is beyond the scope of this thesis to discuss in detail all the processing which was done on the data produced by the experiment, since most of it was of a bookkeeping nature and had no direct bearing on the physics involved. We simply present here an outline of what was done, with emphasis on those aspects which have some relevance to the interpretation of the results. More details may be found in a number of reports on the subject (*Brown*, 1971a, 1971b, 1972).

The first stages of processing consist of merging experiment data and satellite orbit data, checking for and deleting data of poor quality, and extracting and editing information relevant to the Cerenkov Telescope. This is done primarily to reduce the expense and inconvenience of handling large numbers of tapes, and to put the data in a more convenient form.

The next step is to assign vertical cutoff rigidities. Satellite orbit data are available every 60 seconds; these are interpolated to 15-second intervals, then used to calculate cutoff rigidity from a grid calculated by Shea and Smart (*Shea et al.*, 1965, 1968; *Shea and Smart*, 1967; *Shea*, personal communication, 1971). This grid represents "effective" cutoffs, which are derived by averaging over allowed rigidities in the penumbral region (*Shea et al.*, 1965). The grid we used was modified from a 2° by 2° grid kindly supplied by M. A. Shea (personal communication, 1971). The supplied grid was interpolated from a 5° by 15° grid previously published (*Shea et al.*, 1968). We found it necessary to refine the interpolation in the region bounded by latitudes 0°-30°N and longitudes 245°-325°E, using the 5° by 5° grid

calculated by Shea and Smart in that region, as well as points calculated at one-degree latitude intervals for longitudes 260°E and 285°E. This was done by hand, using an iterative graphical technique.

Since this grid is calculated for an altitude of 20 km, the cutoff is extrapolated to spacecraft altitude using the relation (*Smart and Shea*, 1967) $P_c \propto L^{-2}$ where L is the McIlwain parameter (*McIlwain*, 1961). Finally, the cutoff rigidities are interpolated to 144 msec intervals and assigned to each analyzed event and each readout of the Čerenkov scaler.

It is difficult to estimate the accuracy of these calculated vertical cutoffs, since few direct measurements exist. One recent pair of measurements near Palestine, Texas (*Pennypacker et al.*, 1973) using a balloon-borne superconducting magnetic spectrometer gives results which agree to within 0.1 GV with the corresponding interpolated grid values. Since the quoted uncertainty in the measurements is 0.1 GV, we consider the agreement to be excellent. However, it remains an open question whether discrepancies might be found at other geographic locations, although the calculations for high latitudes ($P_c \lesssim 1$ GV) are probably not reliable (*Fanselow and Stone*, 1972) due to the neglect of the field due to external currents (*Smart et al.*, 1969). Also, the calculated cutoffs correspond to a quiet geomagnetic field model. We have made no attempt to correct for geomagnetic activity, the effect of which is to lower the cutoffs from the quiet-time values. This effect may be expected to be most pronounced at high latitudes (low cutoffs) resulting in an apparent distortion of the integral rigidity spectra. However,

because the various abundance ratios are nearly independent of rigidity (Figures IV-4, IV-5, and IV-6), distortion of these ratios by fluctuating cutoffs is a second-order effect, and can be neglected without affecting the conclusions of this thesis.

APPENDIX B. Identification of Geomagnetically Trapped Particles

The Caltech Solar and Galactic Cosmic Ray Experiment on OGO-6 consists of three separate charged-particle telescopes which share pulse height analyzers and readout circuitry. In order to understand the response of the Čerenkov Telescope/electronics system, it is necessary to consider the effects of the other two telescopes. For this purpose, it is sufficient to consider the following: 1) the energy ranges and geometrical factors of the telescopes, 2) the way in which events are selected for analysis, 3) the effects of analyzer dead time, 4) the characteristics of the particle fluxes seen by the instrument.

The Range Telescope analyzes electrons with $E \gtrsim 1$ MeV and nuclei with $E \gtrsim 1$ MeV/nucleon, with a geometrical factor decreasing from ~ 1.5 cm^2·ster at low energies to ~ 0.2 cm^2·ster at $E \simeq 300$ MeV/nucleon. It has the same priority for event analysis as the Čerenkov Telescope. The Flare Telescope analyzes protons (17 to 100 MeV) and alphas (70 to 400 MeV), with a geometrical factor of about 0.02 cm^2·ster (*Althouse et al.*, 1967). The Flare telescope has the highest priority for event analysis. The aluminized Mylar window of the Range Telescope failed in January, 1970, causing the front detector to respond to sunlight. This detector was disabled by ground command, and the logic required for event analysis was modified, causing the Range Telescope to analyze electrons with $E \gtrsim 240$ keV after this time.

The pulse-height analysis system is capable of reading out one event every 144 msec. When the spacecraft is in a region of geomagnetically trapped particles, or in the polar regions during a solar flare, the counting rates of some or all of the telescopes are much

higher than this. If the Flare Telescope rate is >>7/sec, all the analyzed events will be Flare events. If the Flare Telescope rate is ≲7/sec, the Range and Čerenkov Telescopes will compete for whatever analyzer time remains according to the ratio of their counting rates. Because the Range and Flare Telescopes have lower energy thresholds than the Čerenkov Telescope, they usually have much higher counting rates in regions of high trapped-particle flux. As a result of this, plus the event-analysis priority given to the Flare Telescope, relatively few Čerenkov Telescope events are analyzed in the trapped-particle regions. We take advantage of this fact to identify and eliminate data which are contaminated by trapped particles, or by solar flare particles in the polar regions.

The quantities R, C, and N, defined in Chapter IV (number of Čerenkov scaler readouts, number of coincidences, number of analyzed events) are accumulated in one-minute intervals. Typical values are $R < 139\ \mathrm{min}^{-1}$; $C \simeq 10\text{-}40\ \mathrm{min}^{-1}$ for galactic cosmic rays, and $C >> 40\ \mathrm{min}^{-1}$ for trapped particles; $N \gtrsim .9C$ for intervals with no trapped particles, and $N \simeq 0$ for intervals containing trapped particles. The ratio N/C is a sensitive indicator of the presence of trapped particles, and can be used in a "yes-no" fashion to determine whether a one-minute interval should be considered contaminated with a significant number of trapped particles. For this purpose, any interval having a low efficiency for event analysis ($N/C < r$) was designated as contaminated, where r is a parameter discussed below.

The sum of 15 months of data is shown in the following figures. Figure B-1a shows the behavior of the quantity C/R as a function of cut-off rigidity (P_c). Notice the pronounced increases in counting rate at $P_c \simeq 1.2$ GV (outer trapping zone, mostly electrons) and at $P_c \simeq 9.9$ GV (inner trapping zone, mostly protons). The same quantity is shown in Figure B-1b, where a distinction has been made between readouts having $N/C < r$ and those having $N/C \geq r$. These are designated as "low analysis-efficiency" data (L) and "high analysis-efficiency" data (H) respectively.

Likewise, the ratio N/C is shown in Figure B-2a for all the data, and in Figure B-2b after making the separation. Notice that N/C is practically constant in the"high efficiency" data. The small variations are due to the use of analyzer time by the other telescopes, and are not directly correlated with the Čerenkov rate. A value of 0.75 for the parameter r was chosen, after some trial and error, to provide the best separation of the behavior of high efficiency and low efficiency C/R and N/C. Lower values allow too much contamination in the high efficiency data; and higher values cause the rejection of too much good data. However, any value of $r \geq 0.25$ rejects the vast majority of contaminated intervals.

Because the maximum counting rate for galactic fluxes is about 40 min^{-1}, and the maximum number of analyzed events is about 417 min^{-1}, the probability is less than 10% that a Čerenkov event will not be analyzed because the analyzers are busy with a previous Čerenkov event. Thus, the probability of failing to analyze ten (25%) of the Čerenkov events is less than $0.1^{10} = 10^{-10}$. However, since some of the analyzer

Figure B-1

Number of D2'D3'$\overline{D4}$' coincidences per scaler readout observed as a function of cutoff rigidity. Rigidity bins are 0.08 GV wide.

a. Total of all observations;

b. Observations having high efficiency for event analysis (H) separated from low efficiency data (L). Large fluctuations in the (L) data for $P_c \gtrsim 13$ GV are due to the small number of L-type readouts at high cutoffs.

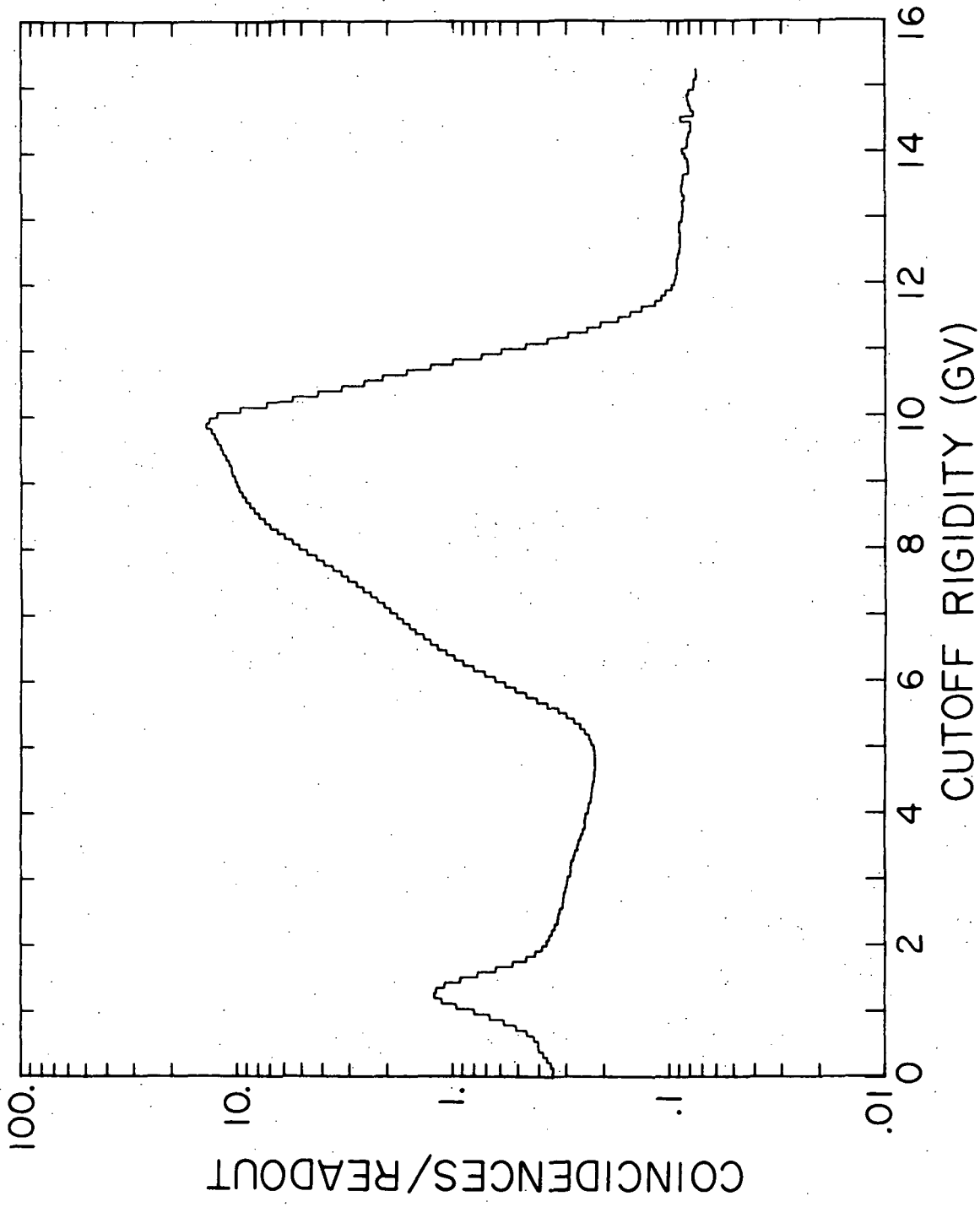
100.
10.
1.
.1
.01
COINCIDENCES/READOUT
0
2
4
6
8
10
12
14
16
CUTOFF RIGIDITY (GV)

Figure B-1a

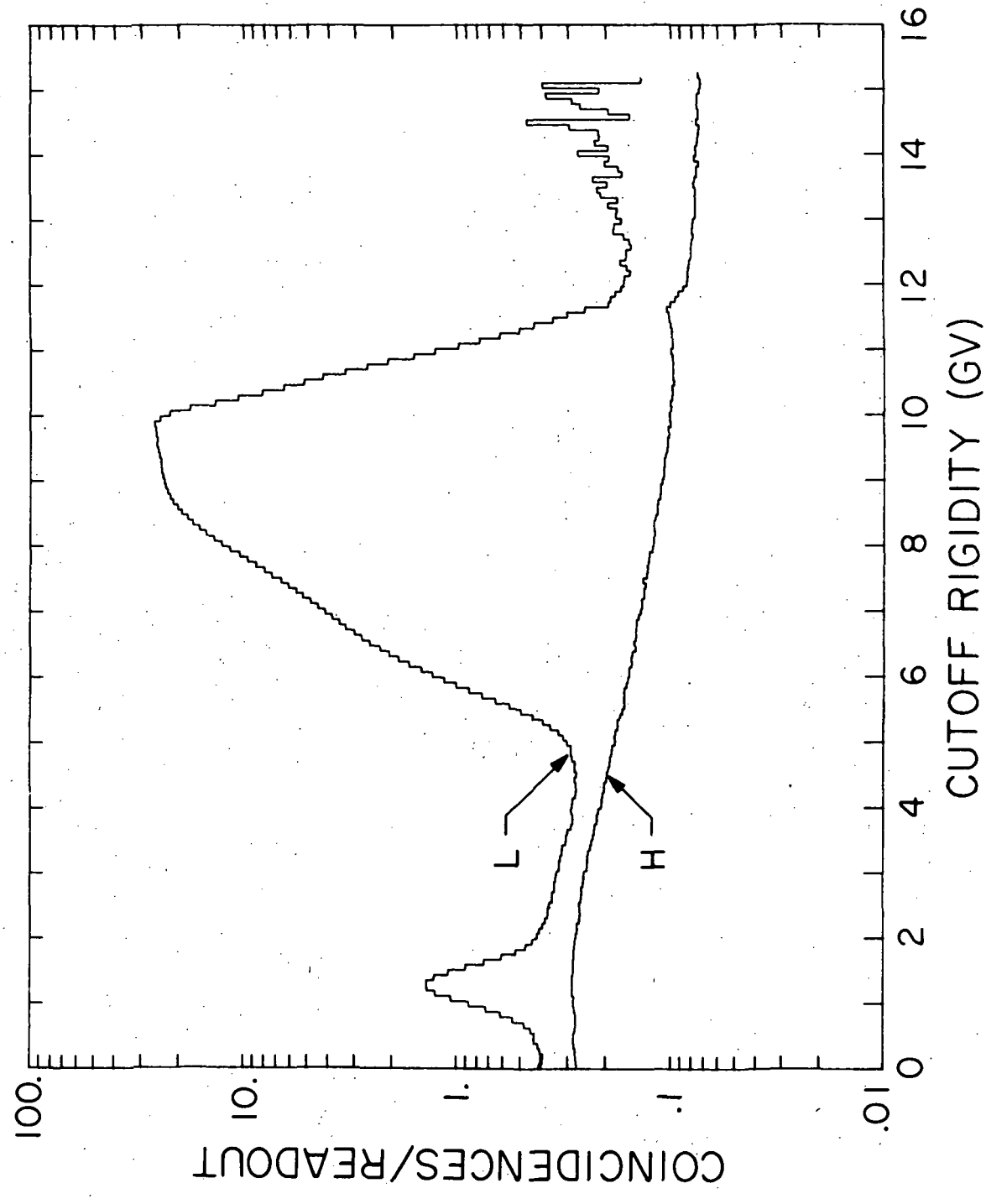
COINCIDENCES/READOUT
100.
10.
1.
.1
.01
0
2
4
6
8
10
12
14
16
CUTOFF RIGIDITY (GV)
L
H

Figure B-1b

Figure B-2

Fraction of Čerenkov events analyzed as a function of cutoff rigidity.

a. Total of all data;

b. Low efficiency (L) and high efficiency (H) data shown separately.

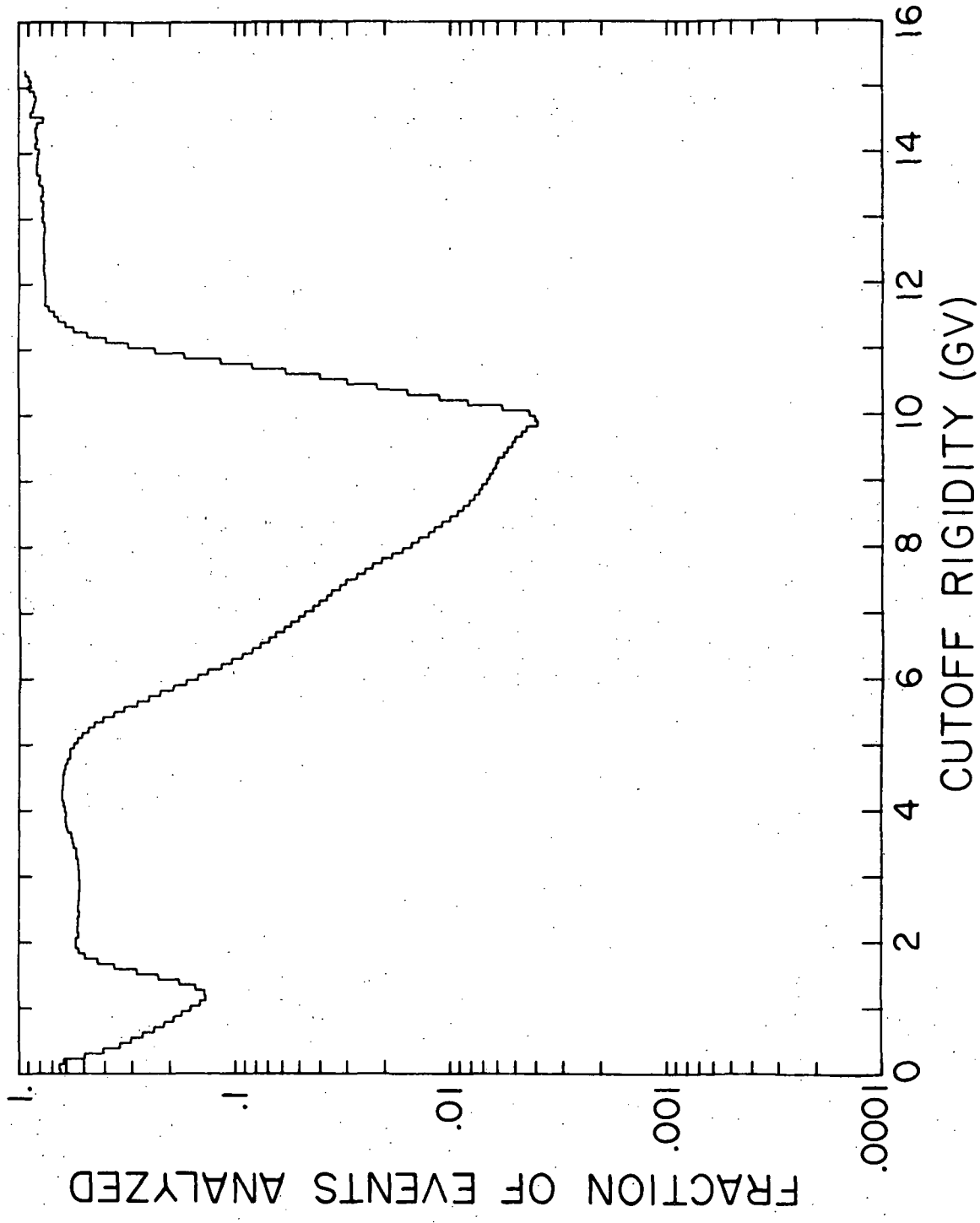
FRACTION OF EVENTS ANALYZED
1.
.1
.01
.001
.0001
0
2
4
6
8
10
12
14
16
CUTOFF RIGIDITY (GV)

Figure B-2a

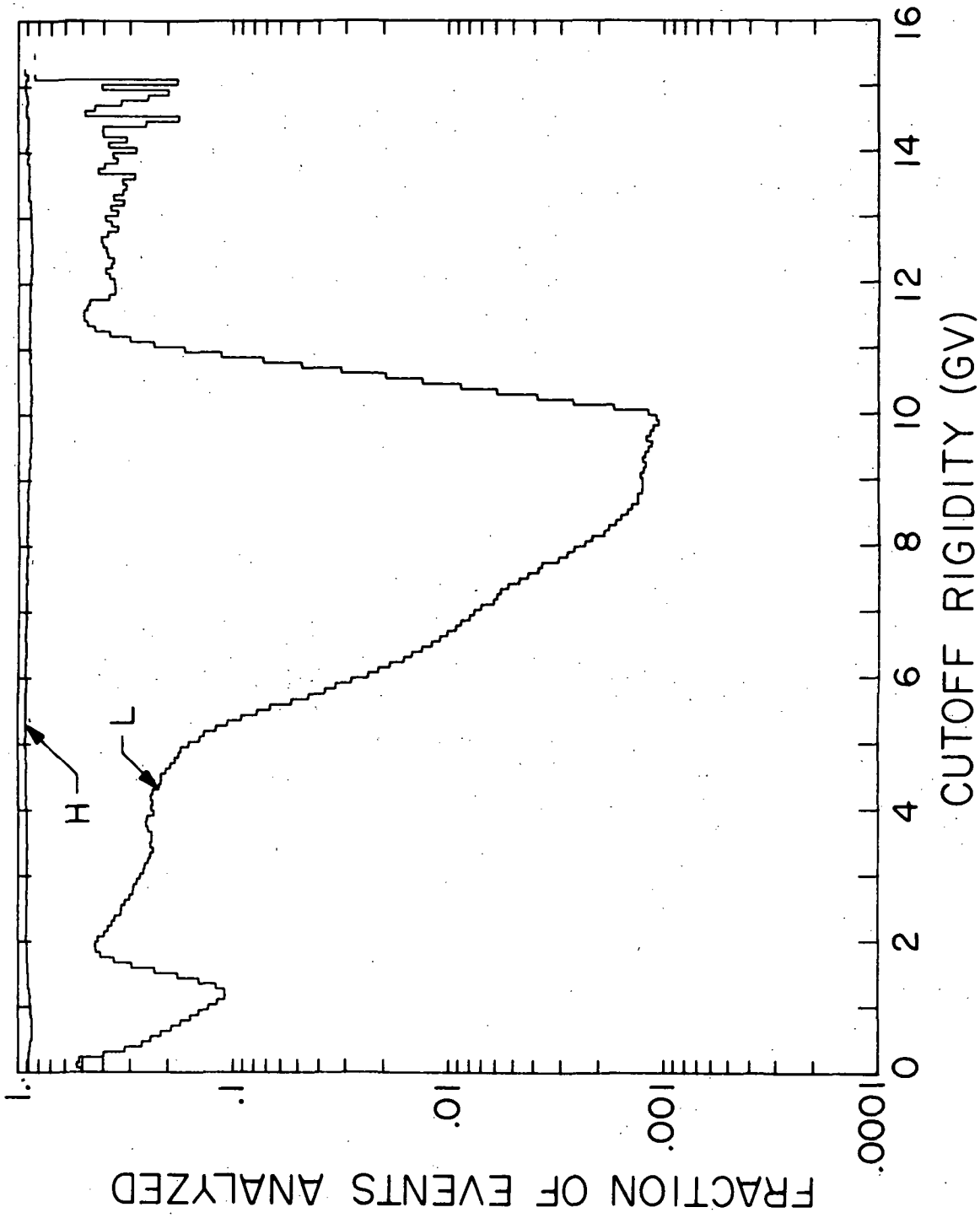
FRACTION OF EVENTS ANALYZED
1.
.1
.01
.001
.0001
0
2
4
6
8
10
12
14
16
CUTOFF RIGIDITY (GV)
H
L

Figure B-2b

capacity is being used by the other telescopes, the actual probability is much higher, resulting in the loss of about 10% of the Čerenkov events, as indicated in the H-curve of Figure B-2b. However, this loss rate is independent of C/R for the high efficiency data.

It can be seen in Figure B-1b that there is some contamination of the high efficiency data by trapped particles at cutoff rigidities between 11 and 12 GV. This must be composed entirely of singly charged particles, since no similar "bump" appears in the helium spectrum of Figure IV-1. In fact, the shape of the total "spectrum" implied by the H-curve in Figure B-1b is substantially different from that of the helium spectrum, due to the large flux of return albedo at high ($\gtrsim$2 GV) cutoffs. For this reason we cannot obtain a spectrum of primary protons. However, the spectra for all $Z > 1$ particles are derived correctly using the method described in Chapter IV, because the albedo and trapped particle fluxes are singly charged. Splash albedo has been measured directly (*Wenzel*, 1968) at Churchill, Canada ($P_c \ll 1$ GV) and Palestine, Texas ($P_c \simeq 4.5$ GV) using an instrument essentially identical to that on OGO-6. The measurements of helium in the splash albedo (T. Garrard, personal communication, 1973) imply an upper limit of $\lesssim 1\ m^{-2}\cdot sec^{-1}\cdot ster^{-1}$ for the integral flux above 300 MeV/nucleon, assuming a differential energy spectrum $\propto E^{-2}$. The spectrum is very likely steeper than that above 300 MeV/nucleon, implying an even smaller upper limit. These considerations indicate that the flux of albedo helium should be $\ll$0.6% of the primary helium flux, causing no ambiguity in the derivation of the primary spectrum. The same considerations presumably apply for heavier nuclei as well. An independent verification

of this conclusion can be obtained by examining event distributions at high cutoffs (*e.g.*, Figure II-5) and noticing that there are no events with low velocities.

The number of scaler readouts R is shown in Figures B-3a, b, and c. The high efficiency readouts in Figure B-3b represent the sampling time available for the analysis done in this thesis.

Figure B-3

Observing time as a function of cutoff rigidity.

a. Total of all observations;

b. Readouts having high efficiency for event analysis;

c. Readouts having low efficiency for event analysis.

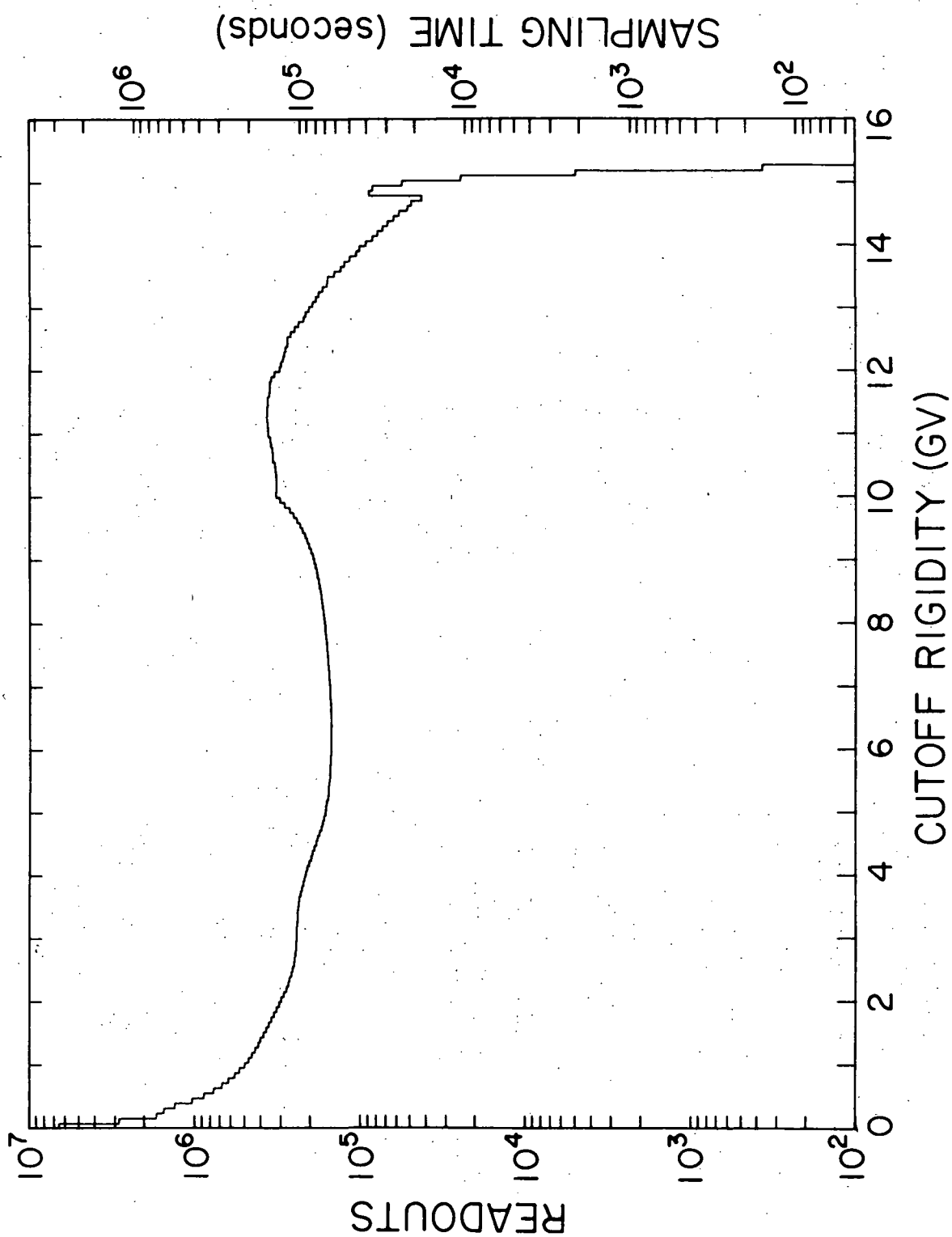
SAMPLING TIME (seconds)
10^6
10^5
10^4
10^3
10^2
16
14
12
10
8
6
4
2
0
CUTOFF RIGIDITY (GV)
10^7
10^6
10^5
10^4
10^3
10^2
READOUTS

Figure B-3a

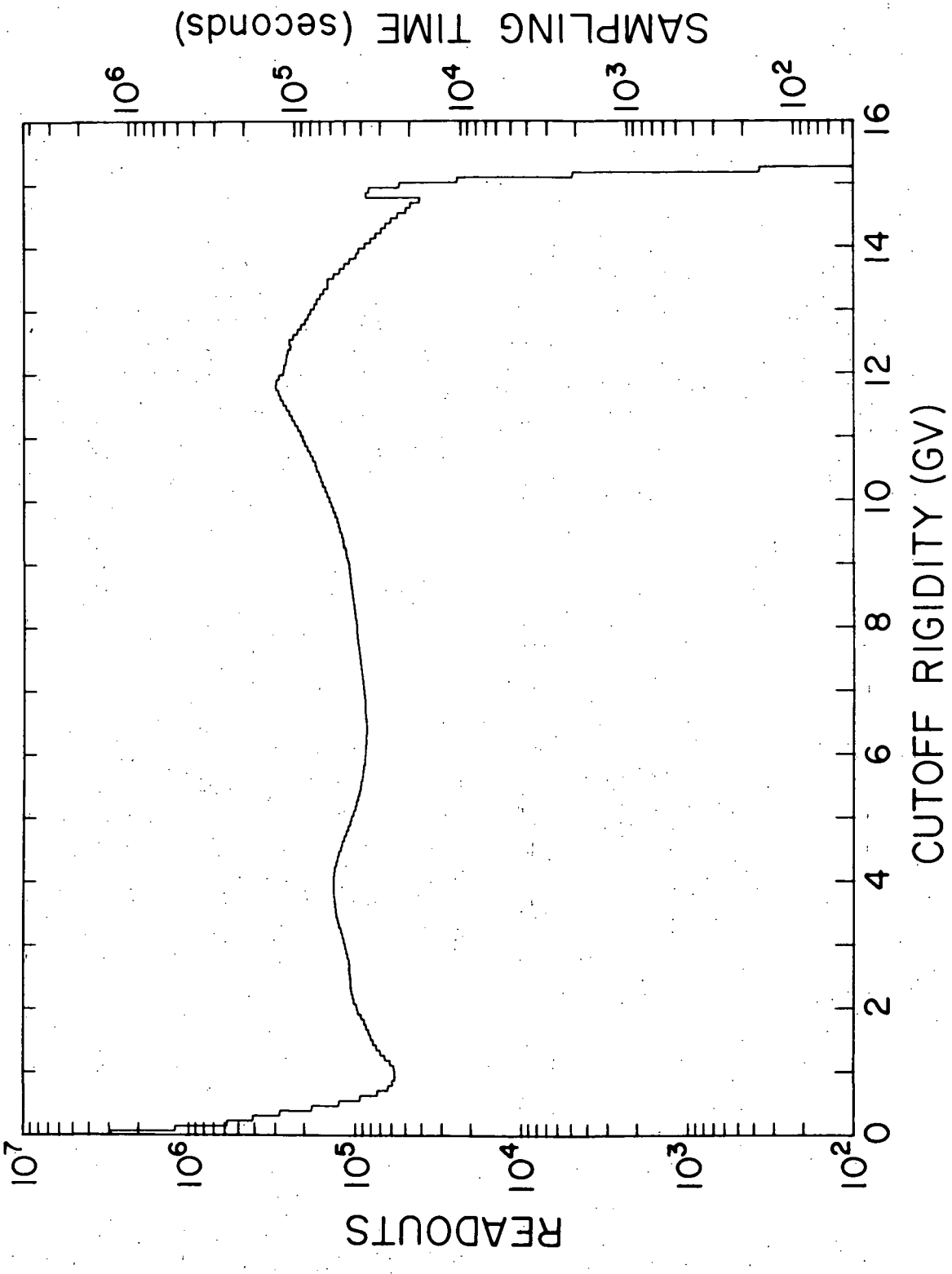
SAMPLING TIME (seconds)
10^6
10^5
10^4
10^3
10^2
16
14
12
10
8
6
4
2
0
CUTOFF RIGIDITY (GV)
10^7
10^6
10^5
10^4
10^3
10^2
READOUTS

Figure B-3b

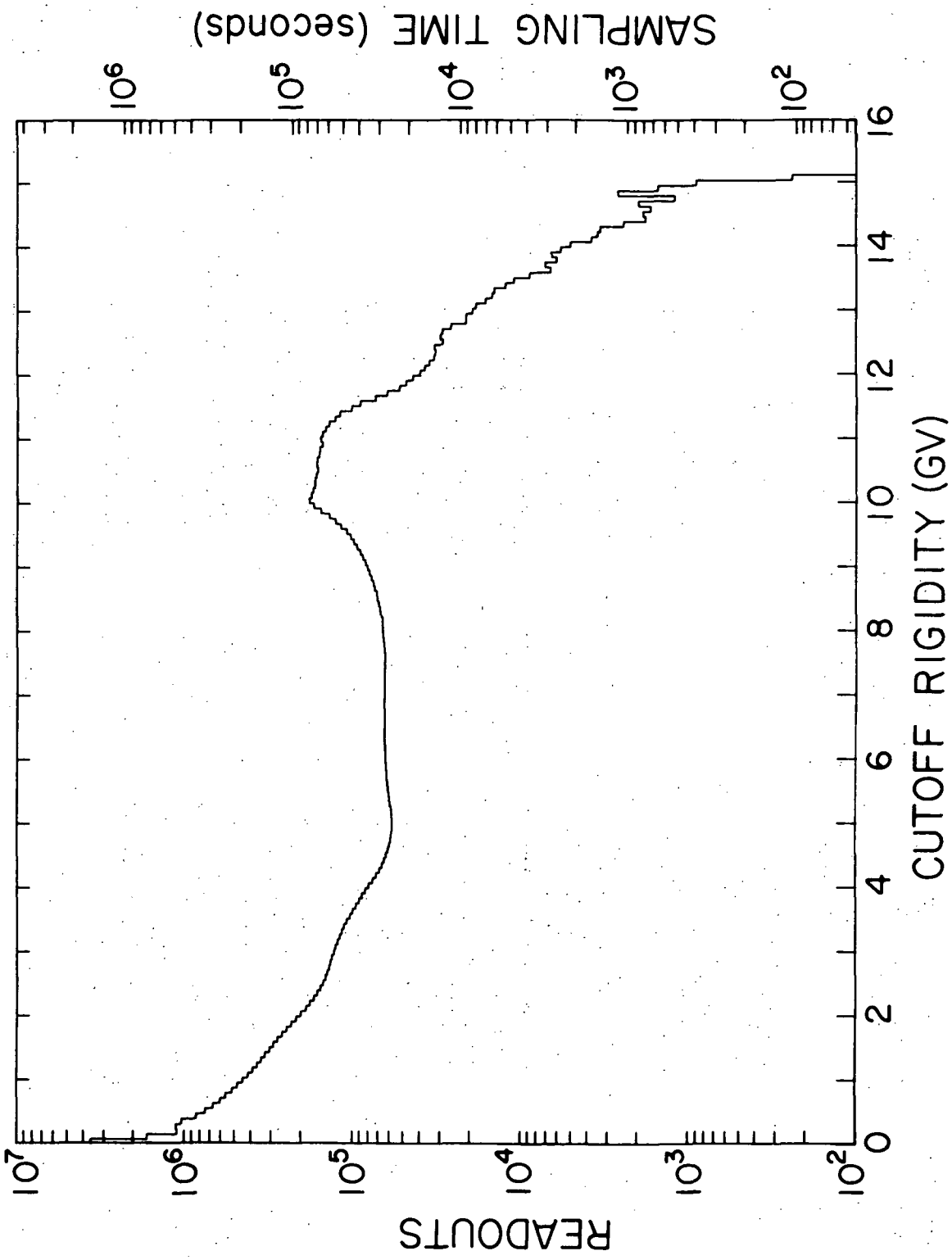
SAMPLING TIME (seconds)
10^6
10^5
10^4
10^3
10^2
CUTOFF RIGIDITY (GV)
0
2
4
6
8
10
12
14
16
READOUTS
10^7
10^6
10^5
10^4
10^3
10^2

Figure B-3c

REFERENCES

Althouse, W. E., E. C. Stone, R. E. Vogt, and T. H. Harrington, "A Solar and Galactic Cosmic Ray Satellite Experiment," *IEEE Trans. Nuc. Sci.*, *15*, 229, 1967.

Balasubrahmanyan, V. K., D. E. Hagge, G. H. Ludwig, and F. B. McDonald, "The Multiply Charged Primary Cosmic Radiation at Solar Minimum, 1965," *J. Geophys. Res.*, *71*, 1771, 1966.

Brown, J. W., "OGO-6 Data Tape Formats," Space Radiation Laboratory Internal Report #24, Calif. Inst. of Technology, Pasadena, 1971a.

Brown, J. W., "User's Guide to OGO-6 Cerenkov Tapes," Space Radiation Laboratory Internal Report #29, Calif. Inst. of Technology, Pasadena, 1971b.

Brown, J. W., "Data Formats for OGO-6 Cerenkov Data Processing," Space Radiation Laboratory Internal Report #40, Calif. Inst. of Technology, Pasadena, 1972.

Cleghorn, T. F., "The Energy Dependence of the Fragmentation Parameters and Interaction Mean Free Paths in Nuclear Emulsion for Heavy Cosmic Ray Nuclei," U. Minn. Cosmic Ray Tech. Rept. CR-104, 1967.

Comstock, G. M., C. Y. Fan, and J. A. Simpson, "Abundances and Energy Spectra of Galactic Cosmic-Ray Nuclei above 20 MeV per Nucleon in the Nuclear Charge Range $2 \leq Z \leq 26$," *Astrophys. J.*, *146*, 51, 1966.

Corydon-Petersen, O., B. Dayton, N. Lund, K. Melgaard, K. Omø, B. Peters, and T. Risbo, "Design and Performance of an Instrument for Determining the Chemical Composition of Primary Cosmic Radiation," *Nuc. Instr. Meth.*, *81*, 1, 1970.

Cowsik, R., Yash Pal, S. N. Tandon, and R. P. Verma, "Steady State of Cosmic-Ray Nuclei--Their Spectral Shape and Path Length at Low Energies," *Phys. Rev.*, *158*, 1238, 1967.

Cummings, A. C., "A Study of Cosmic-Ray Positron and Electron Spectra in Interplanetary and Interstellar Space and the Solar Modulation of Cosmic Rays," Ph.D. Thesis, Calif. Inst. of Technology, 1973.

Evans, R. D., *The Atomic Nucleus*, McGraw-Hill, New York, 1955.

Fanselow, J. L. and E. C. Stone, "Geomagnetic Cutoffs for Cosmic-Ray Protons for Seven Energy Intervals between 1.2 and 39 MeV," *J. Geophys. Res.*, *77*, 3999, 1972.

Pennypacker, C. R., G. F. Smoot, A. Buffington, R. A. Muller, and L. H. Smith, "Measurement of Geomagnetic Cutoff Rigidities and Particle Fluxes below Geomagnetic Cutoff near Palestine, Texas," *J. Geophys. Res.*, *78*, 1515, 1973.

Shapiro, M. M. and R. Silberberg, "Heavy Cosmic-Ray Nuclei," *Ann. Rev. Nuc. Sci.*, *20*, 323, 1970.

Shapiro, M. M., R. Silberberg, and C. H. Tsao, "The Distribution Function of Cosmic-Ray Path Length," *Acta Phys. Acad. Scient. Hungaricae*, *29*, *Suppl.1*, 471, 1970.

Shapiro, M. M., R. Silberberg, and C. H. Tsao, "Revised Source Composition of Cosmic Rays from Hydrogen to Nickel," *The 12th International Conference on Cosmic Rays*, *1*, 221, Univ. of Tasmania, Hobart, 1971.

Shea, M. A. and D. F. Smart, "Worldwide Trajectory-Derived Vertical Cutoff Rigidities and Their Application to Experimental Measurements," *J. Geophys. Res.*, *72*, 2021, 1967.

Shea, M. A., D. F. Smart, and J. R. McCall, "A Five Degree by Fifteen Degree World Grid of Trajectory-Determined Vertical Cutoff Rigidities," *Can. J. Phys.*, *46*, S1098, 1968.

Shea, M. A., D. F. Smart, and K. G. McCracken, "A Study of Vertical Cutoff Rigidities Using Sixth Degree Simulations of the Geomagnetic Field," *J. Geophys. Res.*, *70*, 4117, 1965.

Silberberg, R. and C. H. Tsao, "Calculations of Cross Sections and Their Application to Cosmic-Ray Physics," *The 12th International Conference on Cosmic Rays*, *1*, 273, Univ. Tasmania, Hobart, 1971.

Smart, D. F. and M. A. Shea, "A Study of the Effectiveness of the McIlwain Coordinates in Estimating Cosmic-Ray Vertical Cutoff Rigidities," *J. Geophys. Res.*, *72*, 3447, 1967.

Smart, D. F., M. A. Shea, and R. Gall, "The Daily Variation of Trajectory-Derived High-Latitude Cutoff Rigidities in a Model Magnetosphere," *J. Geophys. Res.*, *74*, 4731, 1969.

Smith, L. H., A. Buffington, G. F. Smoot, L. W. Alvarez, and M. A. Wahlig, "A Measurement of Cosmic-Ray Rigidity Spectra above 5 GV/c of Elements from Hydrogen to Iron," *Astrophys. J.*, *180*, 987, 1973.

Störmer, C., *The Polar Aurora*, Clarendon Press, Oxford, 1955.

Symon, K. R., "Fluctuations in Energy Loss by High Energy Charged Particles in Passing through Matter," Ph.D. Thesis, Harvard U., 1948.

Teegarden, B. J., F. B. McDonald, and V. K. Balasubrahmanyan, "Spectra and Charge Composition of the Low Energy Galactic Cosmic Radiation from Z = 2 to 14," *Acta Phys. Acad. Scient. Hungaricae, 29, Suppl. 1*, 345, 1970.

Von Rosenvinge, T. T., J. F. Ormes, and W. R. Webber, "Measurements of Cosmic-Ray Li, Be, and B in the Energy Range 100 MeV/Nuc to >22 BeV/Nuc," *Astrophysics and Space Science, 3*, 80, 1969.

Webber, W. R., S. V. Damle, and J. Kish, "Studies of the Chemical Composition of Cosmic Rays with Z = 3-30 at High and Low Energies," *Astrophysics and Space Science, 15*, 245, 1972.

Webber, W. R., J. A. Lezniak, J. C. Kish, and S. V. Damle, "Evidence for Differences in the Energy Spectra of Cosmic Ray Nuclei," *Nature, 241*, 96, 1973.

Webber, W. R. and J. F. Ormes, "Cerénkov-Scintillation Counter Measurements of Nuclei Heavier Than Helium in the Primary Cosmic Radiation, 1. Charge Composition and Energy Spectra between 200 MeV/Nucleon and 5 beV/Nucleon," *J. Geophys. Res., 72*, 5957, 1967.

Wenzel, K.-P., "Primäre, Sekundäre, und Albedo-Protonen aus der kosmischen Strahlung," Ph.D. Thesis, Ruprecht-Karl-Universität, Heidelberg, 1968.

Yiou, F. and G. Raisbeck, "Half-Life of ^{10}Be," *Phys. Rev. Letters, 29*, 372, 1972.